Spatiotemporal Dynamics of Molecular Pathology in Amyotrophic Lateral Sclerosis

Silas Maniatis*, Tarmo Äijö*, Sanja Vickovic*, Catherine Braine, Kristy Kang, Annelie Mollbrink, Žaneta Andrusivová, Sami Saarenpää, Gonzalo Saiz-Castro, Miguel Cuevas, Aaron Watters, Joakim Lundeberg†, Richard Bonneau†, and Hemali Phatnani†

*These authors contributed equally to this work

†To whom correspondence should be addressed

Paralysis occurring in amyotrophic lateral sclerosis (ALS) results from denervation of skeletal muscle as a consequence of motor neuron degeneration. Interactions between motor neurons and glia contribute to motor neuron loss, but the spatiotemporal ordering of molecular events that drive these processes in intact spinal tissue remains poorly understood[1,2,3,4]. Here, we use a spatially resolved view of disease-driven gene expression changes to stratify these events, reveal the relevant sub-populations of cells involved in each stage of disease progression, and characterize the underlying molecular mechanisms that trigger and drive the course of disease. Based on the well characterized cellular organization of the spinal cord and the importance of intercellular interactions in ALS disease progression, we applied spatial transcriptomics[5,6,7] (ST) to obtain spatially and anatomically resolved quantitative gene expression measurements of mouse spinal cords over the course of disease, as well as in *postmortem* tissue from ALS patients. We developed a novel Bayesian generative model for assembling a spatiotemporal atlas of gene expression in ALS that integrates cell-type, anatomical region, space, and time. We identify novel pathways implicated in ALS progression, key differences between microglia and astrocyte populations at early time-points and in different anatomical regions, and discern several transcriptional pathways shared between murine models of ALS and human *postmortem* spinal cords. We provide a general experimental-computational design for mapping and understanding the transcriptional landscape of diseases in complex tissues. An interactive data exploration portal for our ST analysis is available at als-st.nygenome.org.

ST generates quantitative transcriptome-wide RNA sequencing (RNAseq) data via capture of polyadenylated RNA on arrays of spatially barcoded DNA capture probes[5,6,7]. We applied ST to spatially profile gene expression in lumbar spinal cord tissue sections (L3-L5) from SOD1-G93A (ALS) and SOD1-WT (control) mice at pre-symptomatic, onset, symptomatic, and end-stage time points (Supplementary Table 1). We then applied ST to profile gene expression in *postmortem* lumbar and cervical spinal cord tissue sections from either lumbar or bulbar onset

sporadic ALS patients. We analyzed spatially resolved transcriptome profiles from over 76 thousand ST spots, mapping to ~1200 spinal cord tissue sections of 67 mice, and over 60 thousand ST spots mapping to 80 *postmortem* spinal cord tissue sections from six patients (Supplementary Table 1).

We annotated each ST data point with an anatomical annotation region (AAR) tag, then used these tags to register data to a common coordinate system (Extended Data Fig. 1; Extended Data Fig. 2; Supplementary Table 1). To estimate gene expression levels accurately and detect significant regional, anatomical, and cell type changes in ST data within and between conditions, we formulated a novel hierarchical generative probabilistic model. Our model incorporates spatial data from multiple time points, anatomical locations, and tissue sections, allowing us to study differential expression in distinct AARs within and across conditions (Extended Data Fig. 1).

We corrected for missing data due to undersampling and bias, which has been a major problem in spatial and single cell RNAseq studies. As a result, we reliably quantitated the spatial distribution of 11,138 genes in mouse and 9,624 genes in human spinal cord sections. Furthermore, principal component analysis of the complete mouse ST data reveals that the majority of the variance is explained by spatial location, disease state, and genotype (Extended Data Fig. 3), and not by major batch effects.

Our analysis recapitulates the specific regional and temporal expression patterns for genes with previously described regional expression profiles (*Mbp*, *Ebf1*, and *Slc5a7)*[8,9,10] and roles in ALS progression (*Aif1, Gfap*)[11]. Immunofluorescence (IF) imaging of the protein products of these genes demonstrates spatial concordance with our ST analysis (Fig. 1; Supplementary Tables 2 and 3). Our observations, shown for example by *Fcrls*, *Aif1*, *Gfap* and *Aldh1l1*, suggest that

microglial dysfunction occurs well before symptom onset, precedes astroglial dysfunction in ALS, and that this early microglial dysfunction is proximal to motor neurons (Supplementary Table 3; Extended Data Fig. 4).

To further explore the microglial activation program, we focused on a mechanism involving TREM2 reported in several neurodegenerative disease models[12,13,14]. TREM2 and TYROBP form a receptor complex that can trigger phagocytosis or modulate cytokine signaling when engaged by membrane lipids, or lipoprotein complexes[14,15]. ST analysis suggests the spatiotemporal order of this TREM2-mediated mechanism in ALS; *Tyrobp* is upregulated pre-symptomatically and before *Trem2* in the ventral horn and ventral white matter, *Lpl* and *B2m* are upregulated pre-symptomatically specifically in the ventral horn, while *Apoe* and *Cx3cr1* are not (Fig. 2; Supplementary Table 3; Extended Data Fig. 4). These genes become widely upregulated in spinal cords of symptomatic mice (Supplementary Table 3). Thus, our ST analysis suggests that TREM2/TYROBP mediated signaling is an early step in disease relevant microglial changes in gene expression. Further, the spatiotemporal ordering of gene expression changes that we observe in this mechanism differs from previously reported results utilizing single cell RNA sequencing of sorted microglia[12,13], demonstrating the value of our spatially-resolved high dimensional analyses.

Trem2 mutations are associated with several neurodegenerative diseases[15,16,17,18,19] and, through mTOR signaling in myeloid cells[15],*Trem2* expression modulates autophagy. Mutations in several autophagy related genes are associated with ALS[15]. ST analysis and IF imaging show that genes involved in autophagy and the endolysosomal system are dysregulated in the ALS spinal cord (Extended Data Fig. 5; Supplementary Table 3). Ablation of autophagy by conditional knockout of *Atg7* in cholinergic cells, including motor neurons (ChAT-Cre$^{+/+}$; *Atg7*$^{fl/fl}$; SOD1-G93A), leads to earlier symptom onset but prolonged survival in ALS mice[20]. To

investigate which pathways might link dysfunction in autophagy to motor neuron loss in ALS, we applied our methods to these mice (*Atg7* cKO). As expected, we observe that expression of *Gfap* and *Aif1,* and activity of the TREM2 microglial activation axis, are greatly reduced when autophagy is ablated in motor neurons, particularly in AARs distal to motor neuron somata (Supplementary Table 3).

To spatially resolve cell-type specific activities of disease-relevant pathways in an unbiased manner, we carried out a co-expression analysis of our mouse ST data. We confirmed the attenuated gliosis in *Atg7* cKO[20] and identified 31 major co-expression modules (Methods; Fig. 3a; Supplementary Table 4) of diverse spatiotemporal and pathway activities (Fig. 3b; Extended Data Fig. 6,7a; Supplementary Table 5). Examining these modules in the context of cell-type specific gene expression data[21,22] reveals that many of the modules are comprised of genes selectively expressed in cell types representing distinct but spatiotemporally correlated biological activities (Extended Data Fig. 7b). To dissect the roles of these cell types, we further grouped the genes of each module based on their cell-type specific expression pattern, resulting in submodules (Methods; Fig. 3c; Supplementary Table 6). These submodules enabled the identification of distinct pathway activities in astrocytes, microglia, and endothelial cells during gliosis in disease relevant AARs at key points in disease progression, and revealed regional subpopulations within distinct cell types[16,17] (Fig. 3; Supplementary Table 6). For example, we identified 25 submodules (of a total of 433) that are enriched for astrocyte-expressed genes. These 25 astrocyte submodules are distributed across 20 co-expression modules, and exhibit diverse spatiotemporal and pathway activities (Supplementary Table 6,7; Extended Data Fig. 8). Thus, our ST analysis identifies gene expression programs characteristic of regional astrocyte populations[23] that display disease relevant spatiotemporal dynamics.

Moreover, we can resolve the effect of ablating autophagy in cholinergic neurons on regional astrocyte populations (Extended Data Fig. 6). For example, modules 21 and 22 are strongly affected by ablation of autophagy (Extended Data Fig. 6). Both modules are highly enriched for astrocyte-expressed genes (Supplementary Table 7). Amongst the genes in module 22, *Pten*, *Akt3*, *Kras*, and *Rb1cc1* are of interest, as they are involved in sphingolipid signaling, neurotrophin signaling, EGFR signaling, chemokine, and autophagy pathways. Interestingly, while sphingolipid signaling is perturbed in module 22, sphingolipid metabolism is dysregulated in module 8, which is enriched for microglia-expressed genes and includes *Hexa* and *Hexb*. HEXA and HEXB catalyze ganglioside GM2 breakdown, and are mislocalized in a subset of motor neurons (Extended Data Fig. 5). GM2 retention in lysosomes leads to accumulation of autophagy markers including SQSTM1 (P62), and is neurotoxic[18]. Modules 21 and 22 display similar temporal dynamics but show distinct spatial expression patterns; module 21 differs from module 22 in that it is preferentially expressed in the white matter. Thus, there appear to be two distinct astrocyte gene expression programs that both display transient, AAR specific changes in gene expression, and are upregulated when autophagy is ablated in cholinergic neurons.

To extend our mouse studies to human disease, we applied our ST workflow to human *postmortem* spinal cord (cervical and lumbar) tissue from six ALS patients. Three patients presented clinically with bulbar symptom onset, and three patients presented with lower limb symptom onset. Our analysis recapitulates characteristic spatial expression patterns (neuron-expressed *SNAP25* is preferentially expressed in the grey matter and oligodendrocyte-expressed *PLP1* in the white matter, Extended Data Fig. 9). An unbiased co-expression analysis resulted in 28 expression modules (Extended Data Fig. 10a,b; Supplementary Table 8). The spatial mapping of modules demonstrates AAR characteristic patterns, some of which vary along the rostrocaudal axis (Fig. 4a) or differ between white matter and grey matter (Extended Data Fig. 10b). Moreover, some of these modules have expected spatially localized pathway

activities and share similar pathway activity with the murine ALS model (Extended Data Fig. 10c; Supplementary Table 9). Consistent with previous studies[24], our human data shows variability in gene expression in the ventral horn related to distance from the site of symptom onset (Supplementary Table 10). Several such changes correlate with the changes observed in the ventral horn of ALS mice (Supplementary Table 3,10). For instance, acetylcholinesterase (*ACHE*), the activity of which has been linked to neuromuscular defects in ALS[16,19], shows a consistent pattern across patients and ALS mice (Fig. 4b,c). Taken together, our human dataset demonstrates the feasibility of applying ST[5,6,7] to study complex neurodegenerative diseases using *postmortem* tissue.

This study provides a comprehensive spatiotemporal, transcriptome-wide gene expression dataset with a unique combination of resolution, replication, and biological perturbation. In addition to our experimental roadmap for spatial transcriptomics, we have described key computational advances that increase the effective resolution and reliability of inferences drawn from spatially resolved data. We demonstrate that our procedure scales to real human and clinical settings, and allows us to draw inferences from murine models and test them in clinical samples. As such, we expect the work presented here to be a substantial resource and spur further mapping of the central nervous system and its modes of dysfunction.

Methods

Murine ALS models

B6SJLSOD1-G93A transgenic and SOD1-WT transgenic mice were obtained from Jackson Laboratories (Bar Harbor, ME), and maintained in full-barrier facilities at Columbia University Medical Center in accordance with ethical guidelines established and monitored by Columbia University Medical Center's Institutional Animal Care and Use Committee. SOD1-G93A mice

were monitored closely for onset of disease symptoms, including hindlimb weakness and weight loss. Disease end-stage was defined as the inability to become upright in 15s after being placed on their back. Aged *Atg7*$^{flox/flox}$; ChAT-Cre; SOD1-G93A mice were a generous gift of Tom Maniatis of Columbia University Medical Center.

Spinal cord collections and sectioning for Spatial Transcriptomics analysis

Mice were transcardially perfused with 1X Phosphate buffered saline (PBS) followed by spinal cord dissection. The L3-L5 lumbar region was isolated based upon ventral root anatomy and embedded in Optimal Cutting Temperature (OCT, Fisher Healthcare, USA). The samples were then plunged into a bath of dry ice and pre-chilled ethanol until freezing and stored at -80°C. Postmortem cervical and lumbar spinal cord sections from sporadic ALS patients were obtained from the Target ALS Multicenter Postmortem Core (www.targetals.org). Frozen tissue blocks were then post-embedded in pre-chilled OCT and stored at -80°C. Cryosections were cut at 10µm thickness onto ST slides, and stored at -80°C for a maximum period of 7 days.

Immunostaining and microscopy

Mice were transcardially perfused with 1X PBS followed by 4% buffered paraformaldehyde (Sigma-Aldrich, USA). Spinal cords were dissected and then post-fixed in 4% paraformaldehyde buffered in 1X PBS. The tissues were then cryoprotected in 30% sucrose diluted in 1X PBS, embedded in OCT and stored at −80°C. Cryosections were cut at 10µm thickness onto Superfrost plus slides (VWR International, USA). Sections were blocked in 1X PBS supplemented with 5% donkey serum (Jackson Immunoresearch, USA), 0.5% Bovine Serum Albumin (BSA, Sigma Aldrich, USA) and 0.2% Triton X-100 (Sigma-Aldrich, USA) for 1h at room temperature. This was followed by primary antibody staining at 4°C overnight, washing in 1X PBS with 0.2% Triton X-100 (PBS-T), and then secondary antibody incubation at room temperature for 1h and washed in PBS-T. The slides were mounted in Vectashield (Vector

Laboratories, USA) and cover slipped (VWR, USA). Primary antibodies were diluted 1:250 except for SLC5A7 (EMD Millipore; MAB5514; 1:100), GFAP (Abcam; Ab4674; 1:500), SQSTM1 (Abcam; Ab56416; 1:500) and MBP (Abcam; Ab209328; 1:1000). AIF1, TYROBP, CTSD, and CTSS (Ab178847; Ab124834; Ab75852; Ab18822) antibodies were obtained from Abcam; EBF1 from Millipore (Ab10523); TREM2 from Novus (Af1729); and HEXA from Thermo Fisher Scientific (PA5-45175). Secondary antibodies were Alexa Fluor conjugated and obtained from Jackson ImmunoResearch. Confocal images were acquired on a Zeiss LSM 780 with a 20x/0.8 Plan-APOCHROMAT objective (Carl Zeiss Microscopy, Germany) or a 63x/1.4 Plan-APOCHROMAT objective (Carl Zeiss Microscopy, Germany). Epifluorescence images were acquired using the same system; both fitted with a Zeiss Axiocam 506 mono (Carl Zeiss Microscopy, Germany). Images were processed using Zen 2012 (Carl Zeiss Microscopy, Germany) and Fiji 2.0.0-rc-65/1.15w25. Gamma was adjusted uniformly within experiments for clarity of presentation.

Preparation of quality control and library preparation slides

For quality control experiments and library preparation, the slides were prepared as described previously[5,26]. In short, a poly-dT (IDT, USA) capture sequence was covalently linked to Codelink (Surmodics, USA) activated glass slides, following the manufacturer's guidelines. For library preparation slide production, 33µM spatially barcoded poly-dT20VN oligonucleotides (IDT, USA) were deposited as 100pL droplets onto Codelink slides as suggested by the manufacturer. The array printing was performed by ArrayJet LTH (Scotland, UK) according to the system requirements. Each library preparation slide had a total of 1007 spatially barcoded positions distributed over a ~42mm^2 area printed in six replicates. Each spatially barcoded ST spot had a diameter of 100µm, with a center-to-center distance of 200µm between the spots.

Histology staining and imaging for Spatial Transcriptomics

These steps were described previously[5,26]. Tissue sections were fixed in methanol-free formaldehyde (Thermo Fisher Scientific, USA) buffered in PBS for 10 min. After fixation, the tissues were dried with isopropanol, HE stained and mounted with 85% glycerol. All of the mouse samples were imaged using the Metafer slide scanning platform (v3.12.8 Metasystems, MetaSystems GmbH) equipped with a 20x/0.8 Plan-APOCHROMAT (Carl Zeiss Microscopy, Germany) and the resulting images stitched with Vslide (v1.1.115, MetaSystems GmbH). All of the human images were processed as described in the *Immunostaining and microscopy* section. In both cases, images were exported as high-resolution .jpg files used in all the following image processing steps.

Optimization of conditions using fluorescent cDNA

Optimal conditions for spatially barcoded ST experiments were determined separately for mouse and human tissue by generating fluorescently labeled cDNA tissue prints as described in Ståhl *et al*[5]. In short, quality control slides were made as described in *Preparation of quality control and library preparation slides* and human and mouse tissues sectioned. While the fixation and staining conditions remained the same[5], the pre-permeabilization conditions were changed to a 20min 20U collagenase I (Thermo Fisher Scientific, USA) treatment at 37°C. The reaction was substituted with 1X Hank's Balanced Salt Solution without phenol red (Thermo Fisher Scientific, USA) and 20µg BSA (NEB, USA). The pepsin permeabilization conditions were shortened to 6min for mouse samples and 8min for human samples. cDNA synthesis at 42°C overnight was performed supplemented with Cy3-dCTPs (PerkinElmer Inc, USA) to generate and fluorescent print of spatial positions where the cDNA reaction took place. The fluorescent print was imaged using an Agilent high resolution C scanner for microarray imaging (Agilent Technologies, USA) at 10% gain in the Cy3 channel. Images taken during HE imaging and Cy3 imaging were overlaid in Fiji[25] and the fluorescent signal outside the tissue boundaries

measured to < 10%. These optimized pre- and permeabilization conditions were used throughout the study.

In situ Spatial Transcriptomics reactions

These steps were described previously[5] and in *Optimizations of conditions using fluorescent cDNA printing*. In short, collagenase permeabilization was conducted followed by pepsin permeabilization. Reverse transcription was done overnight. Tissue was removed by incubation in proteinase K (Qiagen, Germany) at 56°C for 1h when processing mouse samples or 4h in case of human samples at 2X enzyme amounts. After probe release by a Uracil-Specific Excision Reagent, the resulting spatially barcoded cDNA libraries were collected. The remaining background and unused probes on the array surface were detected by a mix of complementary Cy3-modified surface probes ([CY3]AGATCGGAAGAGCGTCGTGT and [CY3]GGTACAGAAGCGCGATAGCAG; both added at 0.1μM concentration in 1X PBS). The probe reaction was incubated for 10min at room temperature; washed in 1X PBS and spun dried before mounting the slide with SlowFade Gold Antifade Mountant (Thermo Fisher Scientific, USA) and imaging. Images were again exported as spots.jpg files.

Spatial Transcriptomics library preparation, sequencing and demultiplexing

These steps were described previously[26] using fragmented and barcoded human RNA as the carrier material. The spike-in constituted around 25% of the libraries. ST cDNA libraries were diluted to 4nM and sequenced on the Illumina NextSeq 550 platform (Illumina, USA) using paired-end sequencing (R1 30bp, R2 55bp). Reads from mouse samples were aligned to the Ensembl mouse genome and transcriptome annotation references (GRCm38.v79) containing the protein-coding genes and lincRNAs whilst excluding mitochondrial transcripts. Reads from the human samples were aligned to the Ensembl human genome and annotation reference (GRCh38.v79) similarly as to the mouse samples. Samples were sequenced at a mean depth of

61.7 million paired-end reads depth which resulted in an average library saturation at 78.1%. The ST Pipeline[27] version 0.8.5 was used in all analyses. The median number of genes and UMI transcripts detected per spatial spot was 1,415 (10th percentile is 490 and 90th percentile is 3,145) and 2,227 (10th percentile is 666 and 90th percentile is 6,348) in mouse and 938 (10th percentile is 419 and 90th percentile is 1,621) and 1,255 (10th percentile is 515 and 90th percentile is 2,409) in human samples, respectively. To focus our analysis on reliably detected genes across spots, we filtered out the genes that were detected in less than 2% of the spots, resulting in 11,140 mouse and 9,627 human genes for subsequent analysis.

Image and Spatial Transcriptomics data processing

HE and Cy3 spots.jpg images were manually aligned using Adobe Photoshop (Adobe Systems, USA) and ST spots underlying the tissue selected. The centroids of the spots were determined using the Fiji "Analyze particles" plugin[25] and the ST pipeline[27] file was the filtered to contain only centroid-adjusted spatial array coordinates and the respective gene-expression count values. In case a sectioning artifact was present, the corresponding ST spot was subtracted from the analyses. This file format was used in all consequent analyses in the study.

Spatial Transcriptomics spot annotation

We designated 11 anatomical annotation regions (AARs) for spinal cord tissue sections (Extended Data Fig. 2a). These regions were designed on the basis of known major functional or molecular divisions. AARs were designed such that the regions could be easily and reliably assigned on the basis of gross morphology and cytology. Each ST spot could be manually assigned with an anatomical region tag. To streamline the annotation process, we developed a custom software with a graphical user interface (https://github.com/simonsfoundation/spatial_transcriptomics_viz) that overlays corresponding ST spot and HE images and enables a quick assignment process of a ST spot to an AAR. The

obtained anatomical annotations were used in the statistical analyses as well as in the tissue registration process described in the following paragraphs.

Detection of individual tissue sections from arrays

To detect separate tissue sections from arrays and link ST spots with tissue sections, we used the following computational approach. First, the detected ST spots were placed on a two-dimensional integer lattice by rounding their x and y coordinates to the nearest integers. Then, the obtained points in the lattice were labeled so that the connected (structure element is [[0,1,0],[1,1,1],[0,1,0]]) regions are assigned the same integer value. Afterwards, tissue sections with less than 10 ST spots were discarded, and the spots with less than 100 (in mouse) and 10 UMIs (in human) were discarded due to the low sequencing depth. Notably, this filtering step can break the neighboring structures of the detected tissue sections and lead to ST spots without any adjacent ST spots, resulting in singular precision matrices (see more on conditional autoregressive prior below; Supplementary Methods). To account for this possibility, we discarded the spots that do not have neighboring spots after filtering (structure element is [[0,1,0],[1,1,1],[0,1,0]]). Finally, all the detected tissue sections were manually checked to ensure their consistency. All the subsequent analyses were done using the original (that is, non-rounded) ST spot coordinates.

Statistical analysis of ST data

For statistical analysis of our ST data we use a hierarchical probabilistic (generative) model that integrates all data simultaneously to correct for undersampling/zero-inflation, model space in both explicit (x,y) and reconstructed (z) dimensions, and model genotype, time and technical effects (https://github.com/tare/Splotch). At the core of the model we use a generalized linear model based using the zero-inflated Poisson (ZIP) distribution with a log link function. We formulate a hierarchical generative probabilistic model with three major components to capture

321 variation in ST data: 1) a linear effect modeling time and biologically driven variation ($\boldsymbol{\beta}$), 2) a
322 spatial random effect, modeling biologically substantive spatial variation (φ), and 3) spot-level
323 variation (ε), modeling spot specific technical variation. Specifically, the rate parameter λ (the
324 quantity of interest for many of the analysis described in this work) of the ZIP likelihoods
325 depends on $\mathbf{x}$, $\boldsymbol{\beta}$, φ, and ε as follows $\log \lambda = \mathbf{x}^T \boldsymbol{\beta} + \varphi + \varepsilon$, where x contains one hot encoded
326 spot annotation (all indices are omitted here for brevity).
327 Next, we will briefly describe these different model components (for complete details of our
328 model, including assumptions and approximations needed for its implementation and code
329 availability and use, see Supplementary Methods). The linear model is built upon the ST spot
330 annotations, and thus its role is to capture offsets (average) in expression of genes in distinct
331 anatomical regions. Importantly, λ captures latent expression levels at individual spots.
332 Moreover, we encode the hierarchical experimental design in the linear model, resulting in a
333 multilevel model that has parameters at different levels representing genotype and time point
334 combinations, sexes, and individuals (e.g. $\boldsymbol{\beta}_{\text{SOD1-WT,p30}} \rightarrow \boldsymbol{\beta}_{\text{Male,SOD1-WT,p30}} \rightarrow (\boldsymbol{\beta}_{\text{Mouse\#1}}, \boldsymbol{\beta}_{\text{Mouse\#2}},$
335 $\boldsymbol{\beta}_{\text{Mouse\#3}})$ in mouse. Whereas, in human we only have two levels so that the first level represents
336 the four different onset (bulbar, lumbar) and sampling location (cervical and lumbar)
337 combinations and the second level is modeling individuals. As a result, the linear model
338 component allows us to share information from multiple tissue sections in model inference to
339 improve the estimation of the model parameters. Clearly, the linear model is not flexible enough
340 to explain the variation in the ST data in full; therefore, we extend the model by adding a spatial
341 random effect (φ) component for capturing remaining spatial correlations. Specifically, we use
342 conditional autoregressive (CAR) prior that has been popular in various spatial data analysis
343 tasks[28],[29]. The adjacency matrices (for the conditional autoregressive prior) representing the
344 correlation structures of the ST spots of all the detected tissue sections were derived using the
345 coordinates of the tissue section ST spots (see above). That is, the possible neighbors of a

346 given ST spot are the nearest ST spots above, below, left, and right on the ST array design.
347 Moreover, the precision and spatial autocorrelation parameters of CAR prior are assigned prior
348 distributions and their posterior distributions are estimated. Our early experiments showed that
349 despite these two spatial model components there was unexplained variation; to account this,
350 we include a spot-level parameter (ε) for modeling remaining variation at the level of individual
351 spots. The parameter (θ^{p}), representing the probability of extra zeros (zero-inflation), and other
352 parameters are given weakly informative priors (Supplementary Methods). Differential exposure
353 of ST spots (sequencing depth) is considered through a size factor s_i as follows $\log(\lambda_i s_i) = \mathbf{x}_i^T \boldsymbol{\beta}$
354 $+ \varphi_i + \varepsilon_i + \log s_i$ (Supplementary Methods); we used the number of UMI counts per spot divided
355 by the median UMI count across spots (2,227 and 1,225 in mouse and human, respectively) as
356 the size factors.
357 Our statistical model was implemented in Stan[30]. Sampling from posterior was done using
358 NUTS (CmdStan 2.16.0) with default settings and running 4 independent chains with 1,000 (500
359 warmup and 500 sampling iterations) iterations per chain. The convergence of the sampling
360 chains was checked using the Gelman-Rubin convergence diagnostic[31]. As genes are
361 independent in our model, we can utilize distributed computing to infer their models. For all
362 considered mouse and human genes, we analyze their full data set simultaneously; that is, for
363 each mouse and human gene, the statistical model is conditioned on 76,136 and 61,031 data
364 points, respectively. This Bayesian inference procedure produces samples for all model
365 parameters from posterior distributions; e.g., we can quantify our knowledge on λ and $\boldsymbol{\beta}$ (at
366 different levels) to allow various subsequent analyses.
367 Studying differential expression at the level of individual spots between tissue sections is
368 impractical due to many reasons, for instance, tissue sections are placed differently on the spot
369 array, variable tissue compositions between tissue sections, random nature of the mRNA
370 capture, and low UMI counts. Therefore, we base our differential expression detection on the 11
371 distinct anatomical regions using the linear model described above. The posterior distributions

of the multilevel latent parameters **β** (11-dimensional vectors) per gene summarize our knowledge on the average expression in different anatomical regions. Notably, due to the relationship between β and λ, a one unit change in β translates to a multiplicative change of e in λ. For instance, by comparing $\boldsymbol{\beta}_{\text{Male,SOD1-WT,p30}}$ and $\boldsymbol{\beta}_{\text{Female,SOD1-WT,p30}}$ we should be able to tell whether the gene of interest is differently expressed between males and females in SOD1-WT at P30. Whereas, $\boldsymbol{\beta}_{\text{SOD1-WT,p70}}$ and $\boldsymbol{\beta}_{\text{SOD1-G93A,p70}}$ should let us detect differentially expressed genes between SOD1-WT and SOD1-G93A at P70. That is, we want to quantify how different two distributions are and give a significance value to the quantified difference. To do this, we take an approach used previously for quantifying differences between posterior distributions, e.g., in order to detect alternative splicing and differential methylation[32,33]. Briefly, we define a random variable $\Delta_\beta = \beta_1 - \beta_2$ (in this study we only compare one-dimensional distributions) and derive its prior and posterior distributions. The posterior distribution of Δ_β is estimated using the posterior samples of β_1 and β_2. If the posterior distribution of Δ_β has a significant probability density around zero, then it suggests that the posterior distributions β_1 and β_2 are similar. To estimate the significance to this, we use the Savage-Dickey density ratio to compare densities of Δ_β at zero before and after observing data $p(\Delta_\beta=0)/p(\Delta_\beta=0|D)$. The $p(\Delta_\beta=0|D)$ values are obtained by evaluating the kernel density estimated probability density functions (scipy.stats.gaussian_kde with the Scott bandwidth estimator). Whereas, the term $p(\Delta_\beta=0)$ can be obtained analytically from prior. The Savage-Dickey density ratio approximates Bayes factors, and thus we can use Jeffreys' interpretation[34] to assess obtained values.

Detecting differential expression between conditions

To detect differentially expressed genes between conditions, we study the posterior samples of **β** coefficients. For instance, in order to to find the genes that are specifically (up or down) expressed in the ventral horn at P30 in SOD1-WT compared to SOD1-G93A we compare the posterior samples $\{\beta_{\text{ventral horn,SOD1-WT,p30}}\}_{1..\text{samples}}$ and $\{\beta_{\text{ventral horn,SOD1-G93A,p30}}\}_{1..\text{samples}}$ using the

Savage-Dickey density ratio. Similarly, to detect genes that are differentially expressed between P70 and P100 in the ventral lateral white in SOD1-G93A we compare $\{\beta_{\text{ventral lateral white,SOD1-G93A,p70}}\}_{1..\text{samples}}$ and $\{\beta_{\text{ventral lateral white,SOD1-G93A,p100}}\}_{1..\text{samples}}$.

Detecting regional differential expression

To detect genes with specific regional expression patterns, we study the posterior samples of **β** coefficients. For instance, genes that are specifically (up or down) expressed in the ventral horn compared to all the other annotation categories (Extended Data Fig. 2a) at P30 in SOD1-WT can be detected by comparing the posterior samples $\{\beta_{\text{ventral horn,SOD1-WT,p30}}\}_{1..\text{samples}}$ and $\{\beta_{\text{medial grey,SOD1-WT,p30}}, \beta_{\text{dorsal horn,SOD1-WT,p30}}, \beta_{\text{ventral medial white,SOD1-WT,p30}}, \beta_{\text{ventral lateral white,SOD1-WT,p30}}, \beta_{\text{medial lateral white,SOD1-WT,p30}}, \beta_{\text{dorsal medial white,SOD1-WT,p30}}, \beta_{\text{central canal,SOD1-WT,p30}}, \beta_{\text{ventral edge,SOD1-WT,p30}}, \beta_{\text{lateral edge,SOD1-WT,p30}}, \beta_{\text{dorsal edge,SOD1-WT,p30}}\}_{1..\text{samples}}$ using the aforedescribed Savage-Dickey density ratio. Whereas, to detect genes that are differentially expressed in the ventral horn compared to other grey matter regions (medial grey and dorsal horn) at P70 in SOD1-G93A we compare the posterior samples $\{\beta_{\text{ventral horn,SOD1-G93A,p70}}\}_{1..\text{samples}}$ and $\{\beta_{\text{medial grey,SOD1-G93A,p70}}, \beta_{\text{dorsal horn,SOD1-G93A,p70}}\}_{1..\text{samples}}$.

Tissue section registration

To register mouse tissue sections, we base our approach on the manual ST spot annotations (assignment to 11 anatomical regions) and the highly stereotypical spinal cord structure. This annotation-based approach is more robust than attempting to register directly HE images of tissue sections of variable (incomplete or disrupted) morphologies. Here, we describe the the registration workflow. First, we attempt to find four centroids for the regions defined by dorsal horn and ventral horn annotated ST spots per detected tissue section (Extended Data Fig. 2d). This is done by applying 2-means clustering on dorsal horn and ventral horn annotated ST spot coordinates separately. To see whether we have detected two separate clusters (likely

representing left and right dorsal/ventral horns), we compute and assess the L2 distances between the centroids of the detected clusters: if the distance is less than 3 (set by inspecting spot distributions on typical tissue sections), then the centroids are not apart, and we have not reliably detected left and right regions. Depending on the starting point and the clustering result we decide how to continue (Extended Data Fig. 2d). Notably, human cervical spinal cord tissue sections are treated differently because of their physical size (Extended Data Fig. 2d). For instance, if we have detected left and right dorsal horns and left and right ventral horns, then we transform the spatial coordinates of the ST spots for each tissue section by rotation such that the dorsal horn and ventral horn centroids respectively align on the vertical axis, and the dorsal horn centroids are above the ventral horn centroids (Extended Data Fig. 2d). After the rotation step, we translate the ST spot coordinates such that a position equidistant from these centroids is at the origin of the coordinate system (Extended Data Fig. 2d). Finally, all the registered tissue sections were manually checked to ensure their accuracy.

Spatiotemporal and disease-dependent co-expression analysis

To study spatiotemporal and disease-dependent co-expression patterns in mouse spinal cord, we consider all the spot-level estimates (λ) from our statistical model (a matrix with 11,138 rows (genes) and 76,136 columns (spots)). First, we calculate Pearson correlation coefficients across all spots of all pairs of genes, resulting in an 11,138 by 11,138 correlation matrix. Next, we apply hierarchical clustering (L1 norm and average linkage) on the correlation matrix to group genes of similar co-expression pattern across genes. The threshold for forming flat clusters was selected so that the main blocks on the diagonal belong to separate clusters.

To study the detected co-expression modules more closely, we visualize registered spatiotemporal and disease-dependent expression patterns. However, we should not directly calculate average expression of genes (λ values) as the genes are expressed at different levels;

therefore, we first standardize λ values across spots within genes, and then calculate average expressions of genes of interest across spots.

Co-expression analysis was carried out similarly with human ST data (9,624 genes and 61,031 spots) as with mouse ST data described above, with one exception, the λ values above the 99th percentile for each gene were clipped to the 99th percentile before calculating the correlation matrix. Additionally, we standardize the human λ values across spots within patients for each gene due to the greater biological variation.

Hexagonal binning of ST data

Hexagonal binning of ST data was done as implemented in matplotlib.pyplot.hexbin. The default reduce_C_function (mean) was used. Bins with less than 3 ST spots were discarded in the visualization unless stated otherwise.

Comparison of mouse and human

To study gene expression changes between distal and proximal regions in human, we compare the posterior samples of **β** coefficients representing distal and proximal regions by calculating their posterior difference (Δ_β) distribution per AAR per patient. Analysis is done at the level of patients because of the greater biological variability in humans. A gene is considered to have a consistent regulation pattern across the patients if all the patients' posterior means of Δ_β (distal-proximal) are either > 0.2 or < -0.2. Furthermore, a gene is considered to have a consistent regulation pattern across species if it has consistent regulation pattern in human and the posterior mean of Δ_β (SOD1-WT - SOD1-G93A) in mouse has the same sign as in human (distal-proximal) and the magnitude of Δ_β in mouse is at least 0.5.

Analysis of publicly available data

The table containing the FPKM values for genes across seven cell types in the mouse cerebral cortex generated by Zhang *et al*[21] was downloaded from https://web.stanford.edu/group/barres_lab/brain_rnaseq.html. The FPKM values were used as is. The count table generated by single nucleus RNA sequencing of adult mouse lumbar spinal cord was provided along the publication by the authors[22] . Additionally, Sathyamurthy *et al.*[22] kindly provided cluster assignments (inferred cell types) for each of the cells, which enabled us to calculate average CPM values per gene per inferred cell type.

We calculated scaled average expressions per data set by dividing the average expression values per gene by the maximum average expression values across cell types of the study. We assumed that a gene was not expressed in the data set if the maximum average expression value across cell types was less than 1 and, in that case, the scaled average expression values were set to 0. When comparing our results with the publicly available data, we only considered the genes that were detected by Zhang *et al*[21] and Sathyamurthy *et al*[22].

The hierarchical clustering of the scaled average gene expression values was done using L1 norm and average linkage. The genes were grouped into clusters by using the automatic threshold selection as implemented in scipy.cluster.hierarchy.dendrogram.

For identifying the submodules containing astrocyte-expressed genes we used the mouse cerebral cortex data set by Zhang *et al*[21]. First, we took the aforementioned scaled average gene expression values. Second, we used the Wilcoxon signed-rank test to see whether the submodule is enriched of astrocyte-expressed genes. Specifically, we compared the expression distribution of the genes belonging to the considered co-expression submodule in astrocytes with their expression distributions in neurons, myelinating oligodendrocytes, oligodendrocyte precursors, microglia, endothelial, and newly formed oligodendrocytes. Then, we took the maximum of the obtained six p-values; the considered submodule is enriched of astrocyte-expressed genes only if the maximum p-value is less than 1e-2. The same procedure can be

used to identify submodules enriched of genes that are specifically expressed in other cell types.

Data availability

Raw mouse data has been deposited to NCBI's Sequence Read Archive (SRA) under project ID PRJNA481056. Raw human data has been deposited at New York Genome Center and is available upon request submitted to alsdata@nygenome.org. All processed data and images used in the analyses have been deposited to als-st.nygenome.org. Source Data for Figs. 1-4 is provided with the paper.

References

1. Haidet-Phillips, A. M. *et al.* Astrocytes from familial and sporadic ALS patients are toxic to motor neurons. *Nat. Biotechnol.* **29,** 824–828 (2011).
2. Tripathi, P. *et al.* Reactive Astrocytes Promote ALS-like Degeneration and Intracellular Protein Aggregation in Human Motor Neurons by Disrupting Autophagy through TGF-β1. *Stem Cell Reports* **9,** 667–680 (2017).
3. Endo, F. *et al.* Astrocyte-derived TGF-β1 accelerates disease progression in ALS mice by interfering with the neuroprotective functions of microglia and T cells. *Cell Rep.* **11,** 592–604 (2015).
4. Phatnani, H. P. *et al.* Intricate interplay between astrocytes and motor neurons in ALS. *Proc. Natl. Acad. Sci. U. S. A.* **110,** E756–65 (2013).
5. Ståhl, P. L. *et al.* Visualization and analysis of gene expression in tissue sections by spatial transcriptomics. *Science* **353,** 78–82 (2016).
6. Berglund, E. *et al.* Spatial maps of prostate cancer transcriptomes reveal an unexplored

landscape of heterogeneity. *Nat. Commun.* **9,** 2419 (2018).

7. Asp, M. *et al.* Spatial detection of fetal marker genes expressed at low level in adult human heart tissue. *Sci. Rep.* **7,** 12941 (2017).
8. Kang, S. H. *et al.* Degeneration and impaired regeneration of gray matter oligodendrocytes in amyotrophic lateral sclerosis. *Nat. Neurosci.* **16,** 571–579 (2013).
9. Häring, M. *et al.* Neuronal atlas of the dorsal horn defines its architecture and links sensory input to transcriptional cell types. *Nat. Neurosci.* **21,** 869–880 (2018).
10. Misawa, H. *et al.* Distribution of the high-affinity choline transporter in the central nervous system of the rat. *Neuroscience* **105,** 87–98 (2001).
11. Alexianu, M. E., Kozovska, M. & Appel, S. H. Immune reactivity in a mouse model of familial ALS correlates with disease progression. *Neurology* **57,** 1282–1289 (2001).
12. Krasemann, S. *et al.* The TREM2-APOE Pathway Drives the Transcriptional Phenotype of Dysfunctional Microglia in Neurodegenerative Diseases. *Immunity* **47,** 566–581.e9 (2017).
13. Keren-Shaul, H. *et al.* A Unique Microglia Type Associated with Restricting Development of Alzheimer's Disease. *Cell* **169,** 1276–1290.e17 (2017).
14. Deczkowska, A. *et al.* Disease-Associated Microglia: A Universal Immune Sensor of Neurodegeneration. *Cell* **173,** 1073–1081 (2018).
15. Evans, C. S. & Holzbaur, E. L. F. Autophagy and mitophagy in ALS. *Neurobiol. Dis.* (2018). doi:10.1016/j.nbd.2018.07.005
16. Liddelow, S. A. *et al.* Neurotoxic reactive astrocytes are induced by activated microglia. *Nature* **541,** 481–487 (2017).
17. Wiese, S., Karus, M. & Faissner, A. Astrocytes as a source for extracellular matrix molecules and cytokines. *Front. Pharmacol.* **3,** 120 (2012).
18. Boutry, M. *et al.* Inhibition of Lysosome Membrane Recycling Causes Accumulation of Gangliosides that Contribute to Neurodegeneration. *Cell Rep.* **23,** 3813–3826 (2018).
19. Campanari, M.-L., García-Ayllón, M.-S., Ciura, S., Sáez-Valero, J. & Kabashi, E.

Neuromuscular Junction Impairment in Amyotrophic Lateral Sclerosis: Reassessing the Role of Acetylcholinesterase. *Front. Mol. Neurosci.* **9,** 160 (2016).

20. Rudnick, N. D. *et al.* Distinct roles for motor neuron autophagy early and late in the SOD1 mouse model of ALS. *Proc. Natl. Acad. Sci. U. S. A.* **114,** E8294–E8303 (2017).
21. Zhang, Y. *et al.* An RNA-sequencing transcriptome and splicing database of glia, neurons, and vascular cells of the cerebral cortex. *J. Neurosci.* **34,** 11929–11947 (2014).
22. Sathyamurthy, A. *et al.* Massively Parallel Single Nucleus Transcriptional Profiling Defines Spinal Cord Neurons and Their Activity during Behavior. *Cell Rep.* **22,** 2216–2225 (2018).
23. Morel, L. *et al.* Molecular and Functional Properties of Regional Astrocytes in the Adult Brain. *J. Neurosci.* **37,** 8706–8717 (2017).
24. Ravits, J. Focality, stochasticity and neuroanatomic propagation in ALS pathogenesis. *Exp. Neurol.* **262 Pt B,** 121–126 (2014).
25. Rueden, C. T. *et al.* ImageJ2: ImageJ for the next generation of scientific image data. *BMC Bioinformatics* **18,** 529 (2017).
26. Vickovic, S. *et al.* Massive and parallel expression profiling using microarrayed single-cell sequencing. *Nat. Commun.* **7,** 13182 (2016).
27. Navarro, J. F., Sjöstrand, J., Salmén, F., Lundeberg, J. & Ståhl, P. L. ST Pipeline: an automated pipeline for spatial mapping of unique transcripts. *Bioinformatics* **33,** 2591–2593 (2017).
28. Gelfand, A. E. & Vounatsou, P. Proper multivariate conditional autoregressive models for spatial data analysis. *Biostatistics* **4,** 11–25 (2003).
29. Jin, X., Carlin, B. P. & Banerjee, S. Generalized hierarchical multivariate CAR models for areal data. *Biometrics* **61,** 950–961 (2005).
30. Carpenter, B. *et al.* Stan : A Probabilistic Programming Language. *J. Stat. Softw.* **76,** (2017).
31. Gelman, A. & Rubin, D. B. Inference from Iterative Simulation Using Multiple Sequences.

Stat. Sci. **7,** 457–472 (1992).

32. Katz, Y., Wang, E. T., Airoldi, E. M. & Burge, C. B. Analysis and design of RNA sequencing experiments for identifying isoform regulation. *Nat. Methods* **7,** 1009–1015 (2010).
33. Äijö, T. *et al.* A probabilistic generative model for quantification of DNA modifications enables analysis of demethylation pathways. *Genome Biol.* **17,** 49 (2016).
34. Jeffreys, H. *Theory of Probability*. (Clarendon Press, 1998).

Supplementary Information is linked to the online version of the paper at www.nature.com/nature.

Acknowledgements

The study was supported by Target ALS, The ALS Association (grant number 15-LGCA-234), The Tow Foundation, and the Knut and Alice Wallenberg Foundation. Human *postmortem* tissue was obtained through the Target ALS Multicenter Postmortem Core. We thank G. Akbalik, D. Fagegaltier, J. Gregory, I. Hubbard, D. Kim, and K. Wei of the Center for Genomics of Neurodegenerative Disease at NYGC for manual anatomical annotation and for manuscript discussions. We thank T. Maniatis of Columbia University Medical Center for providing *Atg7* cKO mice. We acknowledge the computational resources provided by the Scientific Computing Core of the Flatiron Institute. We thank the NGI Stockholm and SciLifeLab for providing infrastructure support.

Author information

Reprints and permissions information is available at www.nature.com/reprints

Competing interests

J.L. is an author on a patent applied for by Spatial Transcriptomics AB covering the described technology.

Corresponding author

Correspondence and requests for materials should be addressed to hphatnani@nygenome.org, rb133@nyu.edu, and joakim.lundeberg@scilifelab.se

Affiliations

Center for Genomics of Neurodegenerative Disease, New York Genome Center, New York, NY, USA

Silas Maniatis, Sanja Vickovic, Catherine Braine, Kristy Kang, and Hemali Phatnani

Mortimer B. Zuckerman Mind Brain Behavior Institute, Columbia University, New York, NY, USA

Catherine Braine, Miguel Cuevas, and Hemali Phatnani

Center for Computational Biology, Flatiron Institute, New York, NY, USA

Tarmo Äijö, Aaron Watters, and Richard Bonneau

Broad Institute of MIT and Harvard, Cambridge, MA, USA

Sanja Vickovic

Science for Life Laboratory, Division of Gene Technology, KTH Royal Institute of Technology, Stockholm, Sweden

Sanja Vickovic, Annelie Mollbrink, Žaneta Andrusivová, Sami Saarenpää, Gonzalo Saiz-Castro and Joakim Lundeberg

Stanford University, Department of Bioengineering, Stanford, CA, USA

Joakim Lundeberg

Center for Data Science, New York University, New York, NY, USA

Richard Bonneau

Contributions

H.P., S.M., and S.V. designed the experiments. S.M. and S.V. performed the experiments, with help from C.B., K.K., M.C., and A.M. T. A. developed and implemented the novel Bayesian generative model and the interactive data exploration portal. S.M., T.A. and S.V. analyzed the data. A.W. implemented the ST spot annotation tool. All authors discussed the results and wrote the manuscript. The project was originally conceived by H.P., with input from all authors throughout experimentation and manuscript preparation.

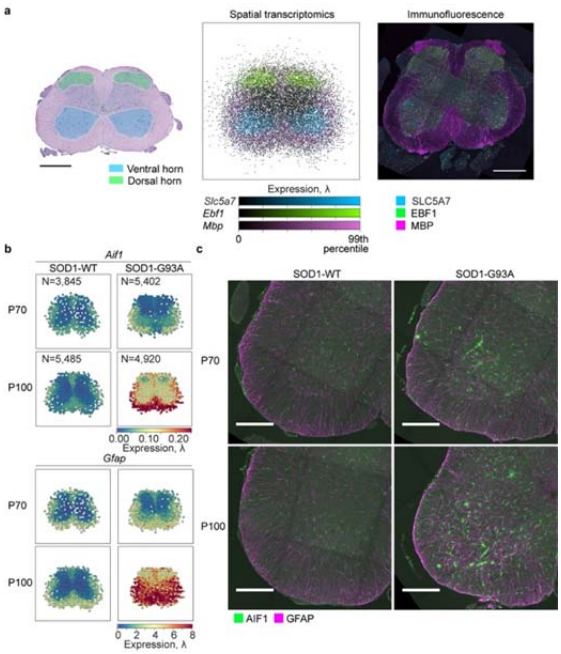

Figure 1. Spatially and temporally resolved gene expression in the mouse spinal cord. (**a**) A schematic diagram of a Hematoxylin and Eosin stained cross-section of mouse lumbar spinal cord with anatomical annotation regions (AARs) overlaid (left panel). Scale bar is 500μm. A multichannel visualization of colocalized spatial mRNA expression of *Ebf1* (green), *Slc5a7* (blue), and *Mbp* (purple) (middle panel). All analyzed and registered ST spots (N=19,380) from the SOD1-WT tissue sections were considered. The posterior means of the rate parameters λ are visualized simultaneously using three colors. Representative Z maximum projection of 10μm confocal image stack of EBF1 (green), SLC5A7 (blue), and MBP (purple) immunofluorescence in mouse lumbar spinal cord (N = 7 animals) (right panel). Scale bar is 500μm. (**b**) Spatial mRNA expression of microglial-expressed *Aif1* and astrocyte-expressed *Gfap* in SOD1-WT and SOD1-G93A lumbar spinal cords at P70 and P100. The value of a bin is calculated as the mean of the ST values (posterior means of λ) within the bin area. The number of ST spots per condition is listed. (**c**) Representative Z maximum projections of 10μm confocal image stacks of AIF1 (green) and GFAP (magenta) immunofluorescence in SOD1-WT and SOD1-G93A spinal cords at P70 and P100 (N = 12 animals). Scale bars are 250μm.

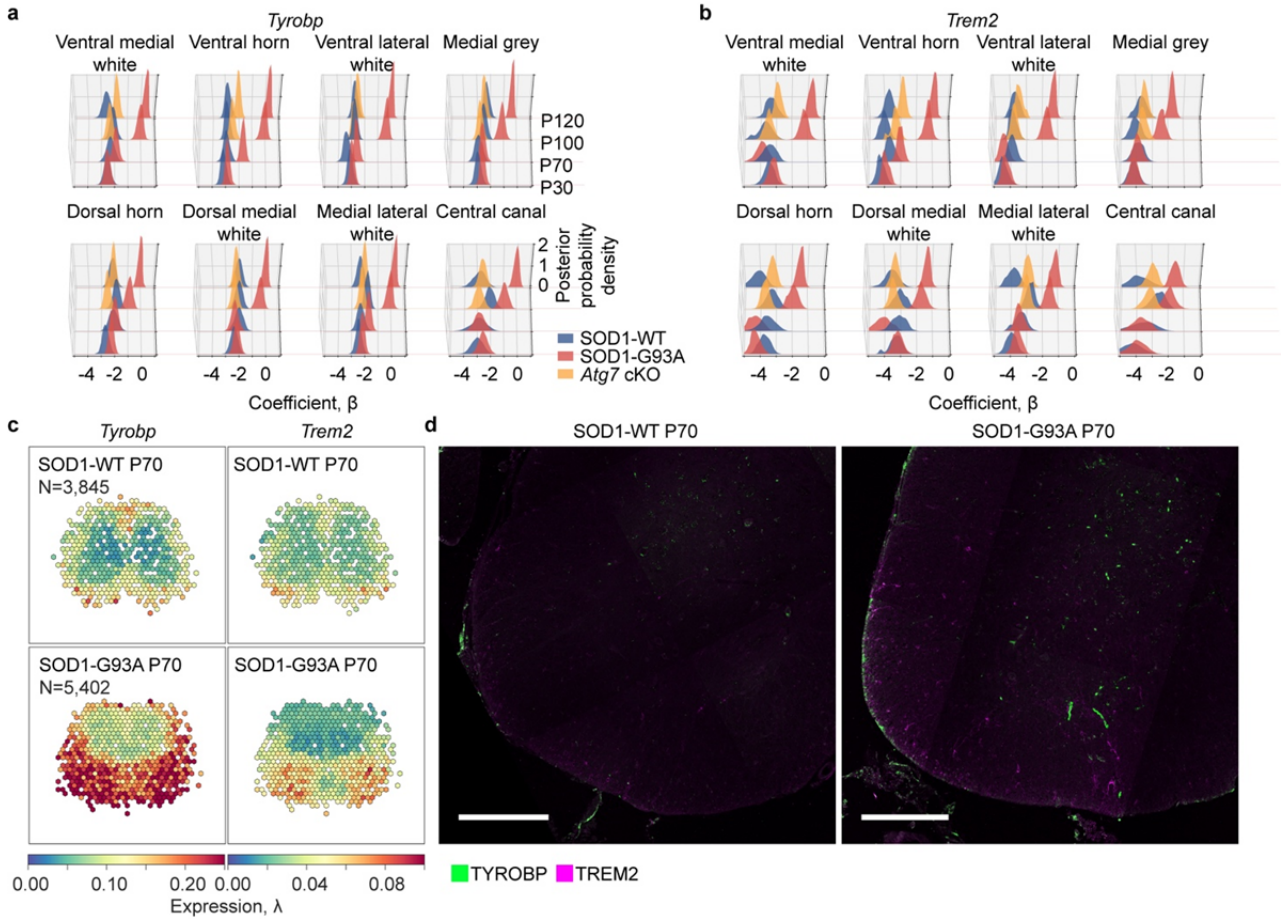

Figure 2. Pre-symptomatic dysregulation of TREM2/TYROBP mediated signaling.

(**a**) The posterior distributions of coefficient parameters β of *Tyrobp* of different AARs in SOD1-WT (blue), SOD1-G93A (red), and *Atg7* cKO (yellow) at P30, P70, P100, and P120. The coefficient parameters β capture offsets of expression (in natural logarithmic space) in distinct AARs across all tissue sections of a given condition. (**b**) As in (**a**), with the focus here on *Trem2*. (**c**) Spatial mRNA expression of *Tyrobp* in SOD1-WT and SOD1-G93A spinal cords at P70. The bin value is the mean of the ST values (posterior means of λ) within the bin area. The number of ST spots per condition is listed. (**d**) Representative Z maximum projections of 10μm confocal image stacks TYROBP (green) and TREM2 (magenta) immunofluorescence in SOD1-WT and SOD1-G93A ventral-lateral spinal cords at P70 (N = 6 animals). The scale bar is 250μm.

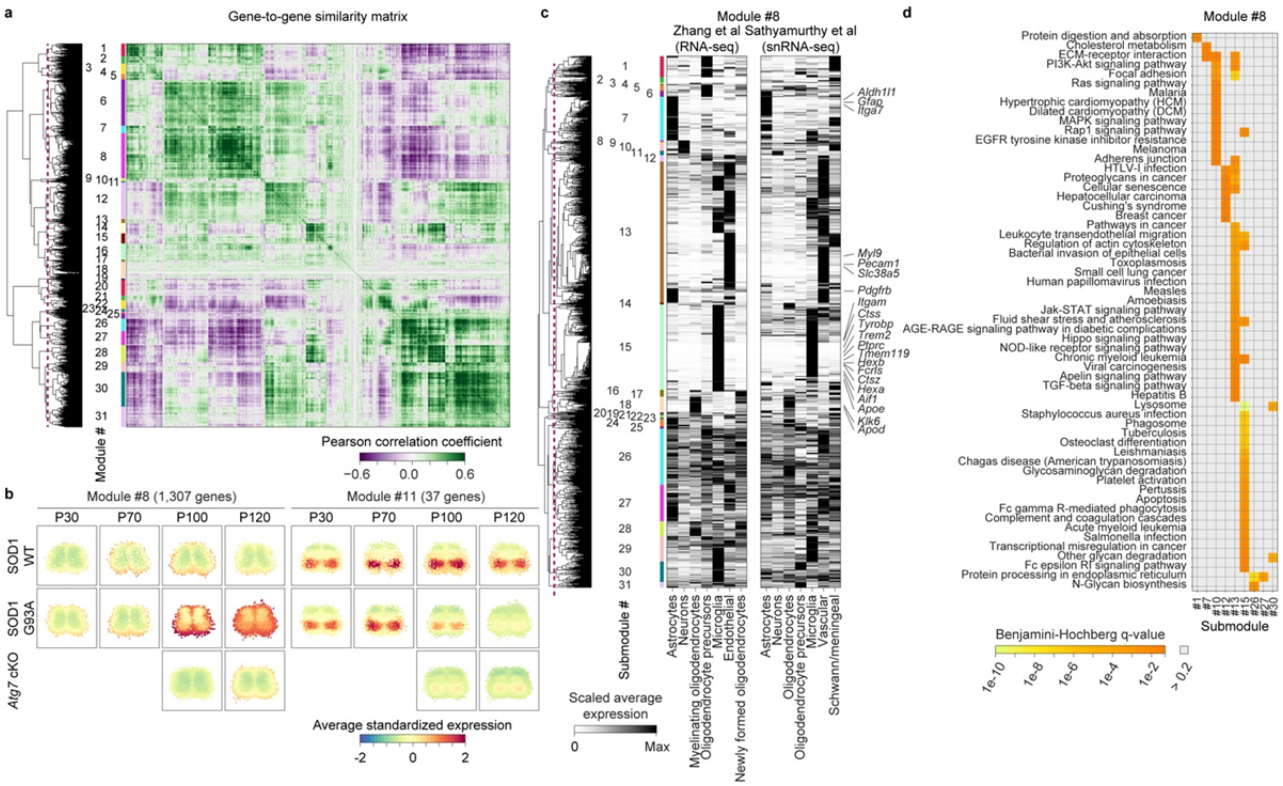

Figure 3. Spatiotemporal dynamics of gene expression during disease progression in ALS.

(**a**) Biclustering of the mouse ST data reveals spatially and temporally co-expressed genes. The dashed vertical purple line in the dendrogram denotes the break. The identifiers given to the co-expression modules are listed. (**b**) Average spatiotemporal expression dynamics of genes in co-expression modules 8 and 11 are visualized. The number of ST spots per condition is listed. (**c**) Analysis of cell type specific expression of genes in co-expression module 8 by hierarchical clustering of the genes using independent gene expression data of brain cell types[21] and spinal cord cell types[22]. The dashed vertical purple line in the dendrogram denotes the break. The identifiers given to the co-expression submodules are listed on right of the dendrogram. Selected genes of interest are highlighted on right. (**d**) Analysis of enriched KEGG pathways among the genes of the submodules depicted in (**c**) (one-tailed Fisher's exact test with Benjamini-Hochberg correction, FDR < 0.1) Adjusted p-values per KEGG category per submodule are shown.

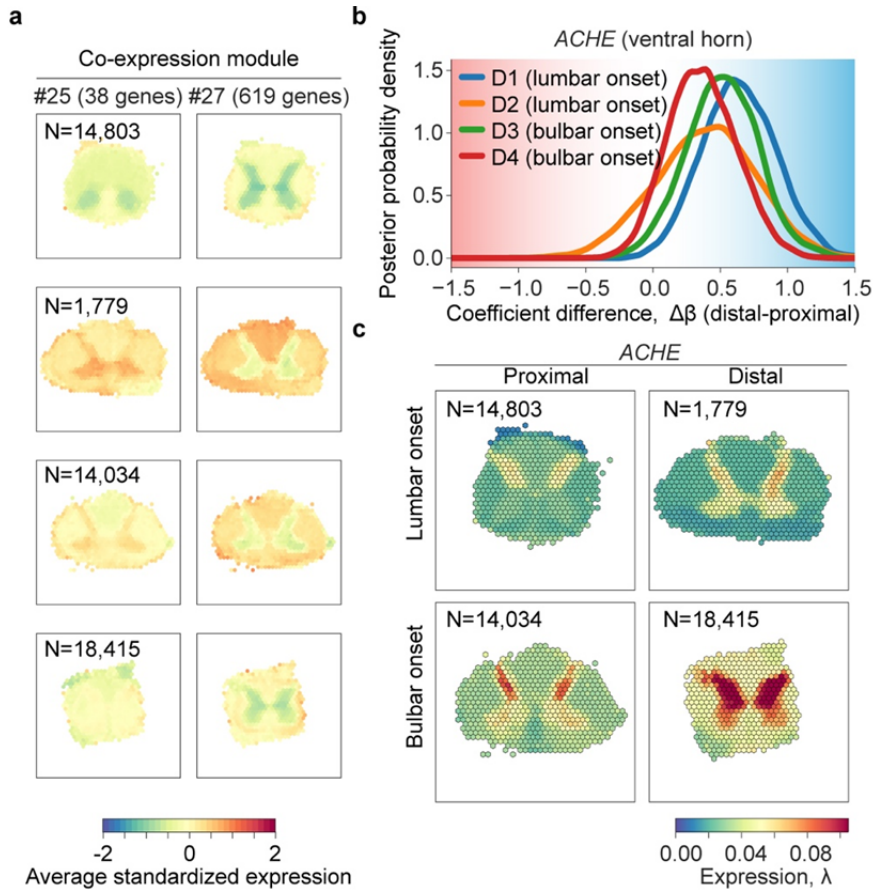

Figure 4. Spatiotemporal transcriptome of human post-mortem spinal cord tissue from ALS patients.

(**a**) Average spatiotemporal expression dynamics of the genes of the human co-expression modules 25 and 27 are visualized. The number of ST spots per condition are listed. (**b**) The posterior difference distributions of the ventral horn coefficients of *ACHE* per patient are visualized. The differences are calculated between the distal and proximal regions with respect to the onset location. The different line colors represent different patients. (**c**) Spatial mRNA expression of *ACHE* in human post-mortem lumbar spinal cord and cervical spinal cord tissue sections are visualized. The proximal and distal regions with respect to the onset location are illustrated separately. The bin value is the mean of the ST values (posterior means of λ) within the bin area. The number of ST spots per condition are listed.

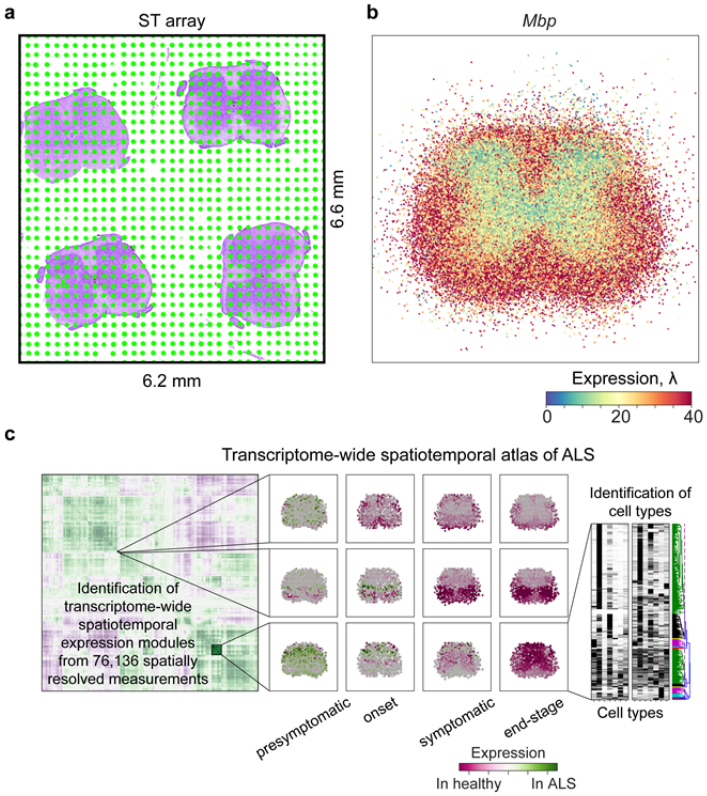

Extended Data Figure 1 | Schematic representation of analytical workflow. Spatially resolved RNAseq data is acquired from discrete ST array features, mapping sparsely onto individual spinal cord sections. Through replication, registration, and standardization, we densely and evenly sample transcriptome-wide expression across the lumbar spinal cord. Using the analytical methods developed in this study, we identify coordinated expression modules that span several cell types. By examining these expression modules in the context of cell-type specific expression data, we narrow the focus to the activities of individual cell types within expression modules. (**a**) Four hematoxylin and eosin stained mouse lumbar spinal cord sections in the context of the ST array used in acquisition of spatially resolved RNAseq data from these sections. (**b**) Spatial expression of *Mbp* from all registered arrays. Expression levels are color encoded from lowest (Green) to highest (Red) for all spots (N=70,523) from all registered arrays, and assigned to a spot drawn at the registered spatial coordinate for each measurement. (**c**) Co-expression analysis identifies coordinated expression modules (left panel). The activities of these modules is examined in their spatiotemporal context, and compared across genotypes (middle panel). Genes comprising one such expression module are examined in the context of cell type specific expression data (right panel).

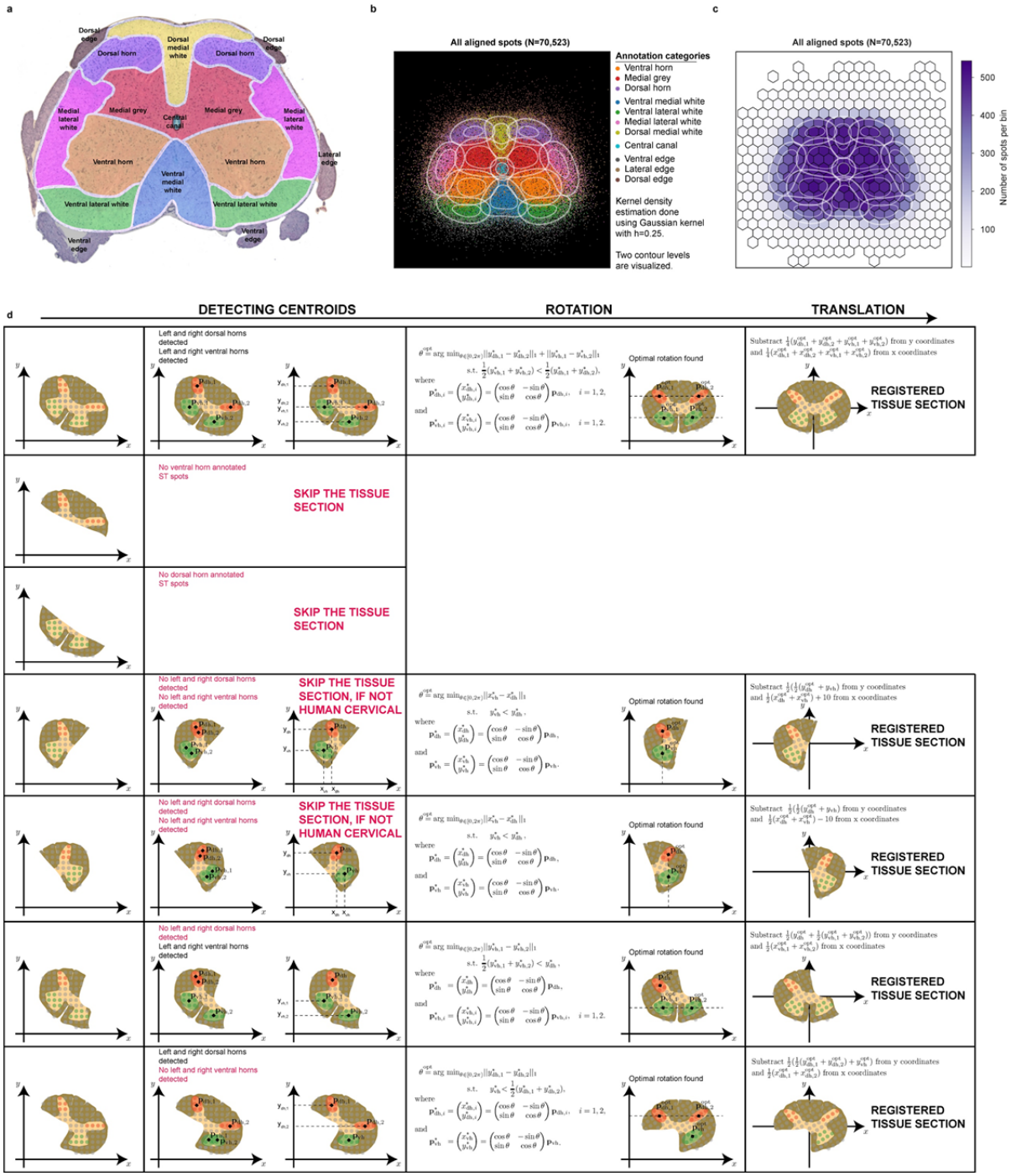

Extended Data Figure 2 | Anatomical annotation regions (AARs) and the procedure to register tissue sections by using AARs. (**a**) A schematic diagram of how the 11 considered AARs were defined. (**b**) Spatial distribution of AARs after the mouse tissue sections have been registered. All the registered mouse tissue sections are considered. The different colors depict different AARs. The contour lines are calculated per AAR. (**c**) Two-dimensional histogram using hexagonal binning summarizing the spatial distribution of registered mouse ST spots. All the registered mouse tissue sections are considered. The contour lines are calculated as in (**b**). (**d**) We consider seven different possible scenarios (on rows) and describe our procedure step-by-step (on columns) separately for those. Each procedure proceeds from left to right. In the case of the scenario depicted on the first row, we identify left and right ventral and dorsal horn centroids using AARs. Then, we rotate tissue sections so that the discrepancies between the y coordinates of the left and right ventral horn and the left and right dorsal horn centroids are minimized. Finally, we translate tissue sections so that they are centered around the origin using the aforementioned AARs. Depending on the case, the aforedescribed procedure is modified as depicted.

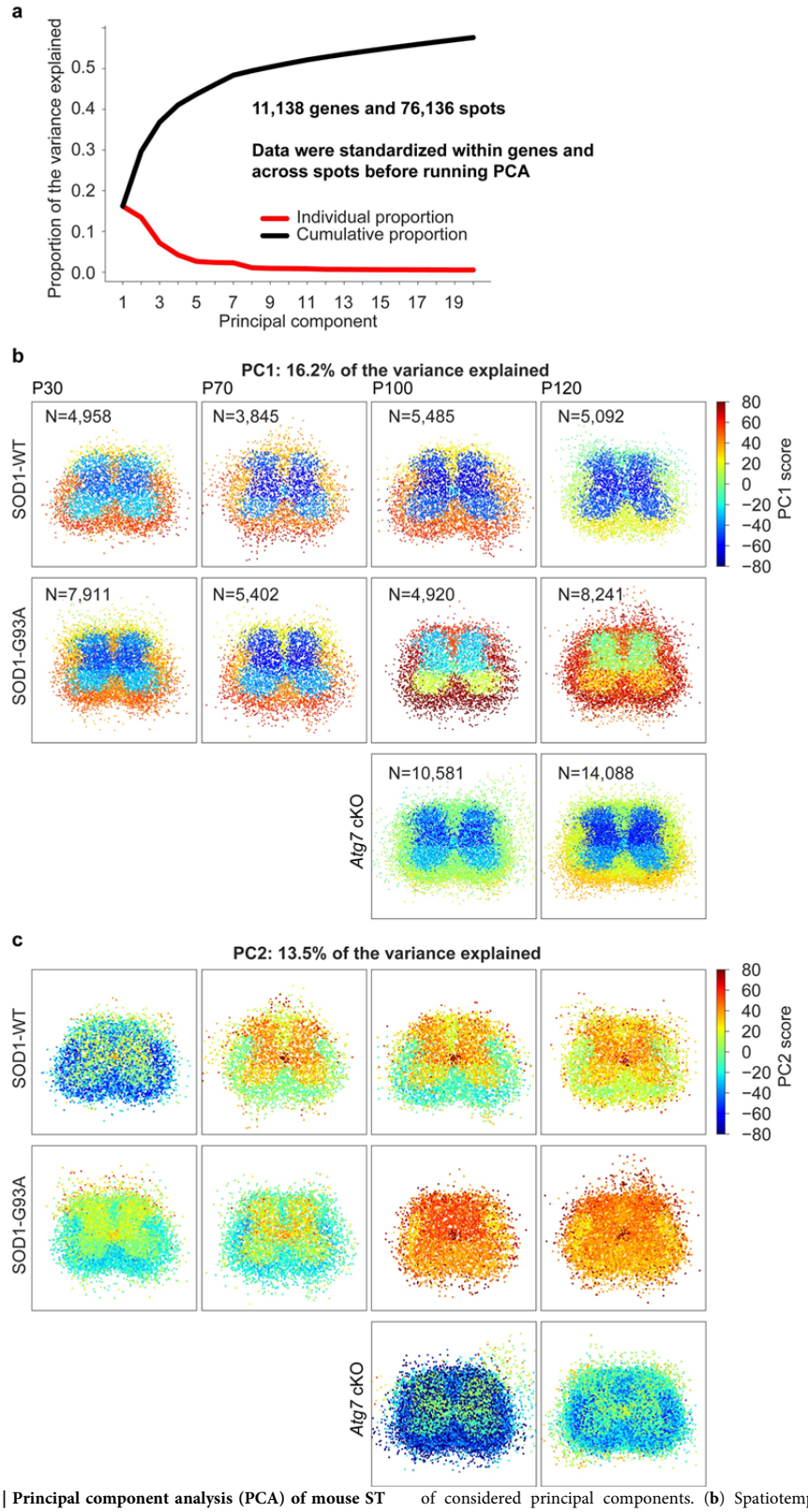

Extended Data Figure 3 | Principal component analysis (PCA) of mouse ST data. (**a**) The percentage of the variance (red curve) explained by each principal component as a function of the principal component number. The cumulative percentage of the variance (black curve) explained as a function of the number of considered principal components. (**b**) Spatiotemporal distribution across genotypes of projected ST data on the first principal component. The number of ST spots for each condition are listed. (**c**) As in (**b**), with the focus here on the second principal component.

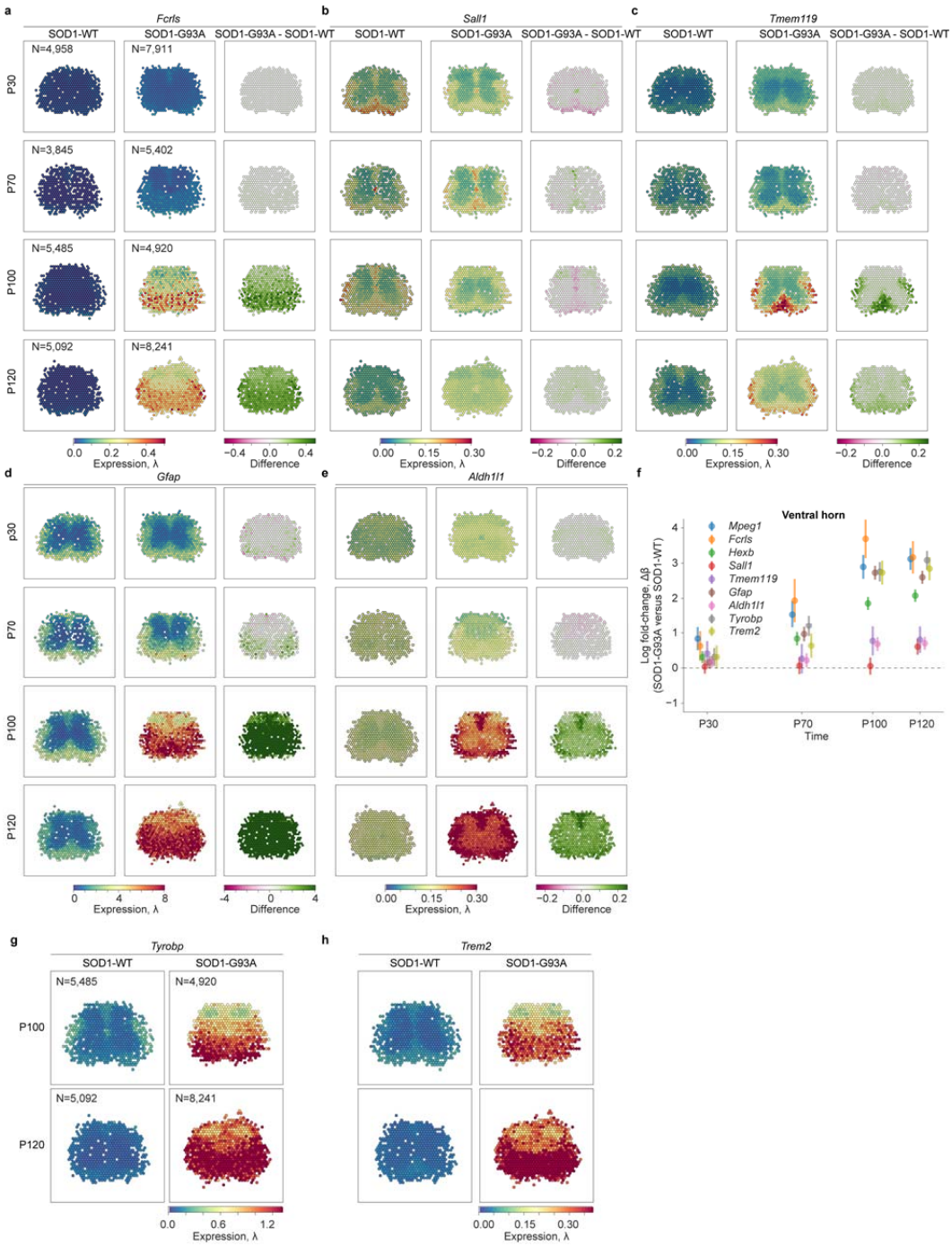

Extended Data Figure 4. Spatiotemporal expression dynamics of *Fcrls*, *Sall1*, *Tmem119*, *Gfap*, *Aldh1l1*, *Tyrobp*, and *Trem2*. (**a**) Spatial mRNA expression of *Fcrls* in SOD1-WT (left panel) and SOD1-G93A spinal cords (middle panel) at P30 (first row), P70 (second row), P100 (third row), and P120 (fourth row). Spatial mRNA expression difference is calculated and illustrated between SOD1-WT and SOD1-G93A per time point (right column). The value of a bin is calculated as the mean of the ST values (posterior means of the rate parameters λ) within the bin area. Bins with less than 3 ST spots are discarded. The number of ST spots per condition are listed. (**b**) As in (**a**), with the focus here on *Sall1*. (**c**) As in (**a**), with the focus here on *Tmem119*. (**d**) As in (**a**), with the focus here on *Gfap*. (**e**) As in (**a**), with the focus here on *Aldh1l1*. (**f**) Temporal dysregulation of *Mpeg1*, *Fcrls*, *Hexb*, *Sall1*, *Tmem119*, *Gfap*, *Aldh1l1*, *Tyrobp*, and *Trem2* in the SOD1-G93A ventral horn is visualized. The values are calculated based on the coefficient data of Extended Data Table 3. That is, we calculated the difference (shown in circles) of the posterior means of the SOD1-G93A and SOD1-WT ventral horn coefficients per time point. The error bars extend to the difference ± the standard deviation, where the square of the standard deviation is the sum of the squares of the standard deviations of the ventral horn coefficient. (**g**) Spatial mRNA expression of *Tyrobp* in SOD1-WT (left panel) and SOD1-G93A spinal cords (middle panel) at P100 (first row) and P120 (second row). The value of a bin is calculated as the mean of the ST values (posterior means of the rate parameters λ) within the bin area. Bins with less than 3 ST spots are discarded. The number of ST spots per condition are listed. (**h**) As in (**g**), with the focus here on *Trem2*.

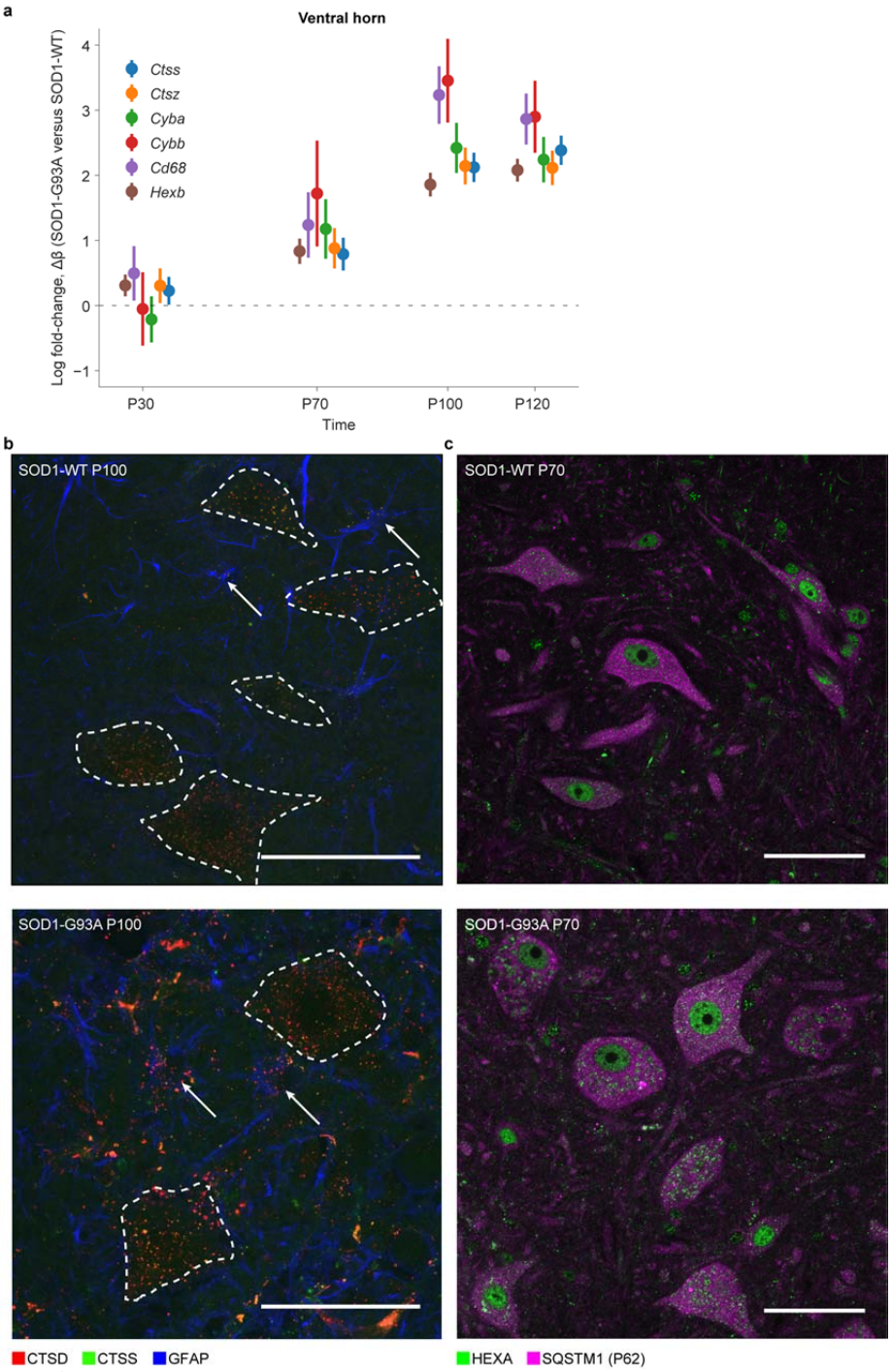

Extended Data Figure 5 | Lysosomal markers are dysregulated and mislocalized in multiple cell types in SOD1-G93A. (**a**) Temporal dysregulation of *Ctss*, *Ctsz*, *Cyba*, *Cybb*, *Cd68*, and *Hexb* in the SOD1-G93A ventral horn is visualized. The values are calculated based on the coefficient data of Extended Data Table 3. That is, we calculated the difference (shown in circles) of the posterior means of the SOD1-G93A and SOD1-WT ventral horn coefficients per time point. The error bars extend to the difference ± the standard deviation, where the square of the standard deviation is the sum of the squares of the standard deviations of the ventral horn coefficient. (**b**) Representative Z maximum projection from 10μm thick confocal image stacks of CTSD (red), CTSS (green), and GFAP (blue) protein immunofluorescence (N = 5 animals). Motor neuron somata (dashed lines) were segmented using TUBB3 immunofluorescence (not shown). Lysosomal markers CTSD and CTSS form large, brightly labeled puncta in motor neuron somata, astrocytes (arrows) and other GFAP negative glial structures in P100 SOD1-G93A spinal cords that are not present in SOD1-WT. (**c**) Representative single confocal image planes of HEXA (green) and SQSTM1 (magenta) immunofluorescence (N = 5 animals). Motor neurons display varying levels of aberrant HEXA protein localization in SQSTM1 negative structures in pre-symptomatic P70 SOD1-G93A spinal cords that are not present in SOD1-WT. SQSTM1 aggregates are also apparent only in SOD1-G93A motor neurons.

Extended Data Figure 6 | Spatial distribution of co-expression modules. Average spatiotemporal expression dynamics of the genes of the co-expression modules depicted in Fig. 3a are visualized. The number of genes per co-expression module are listed.

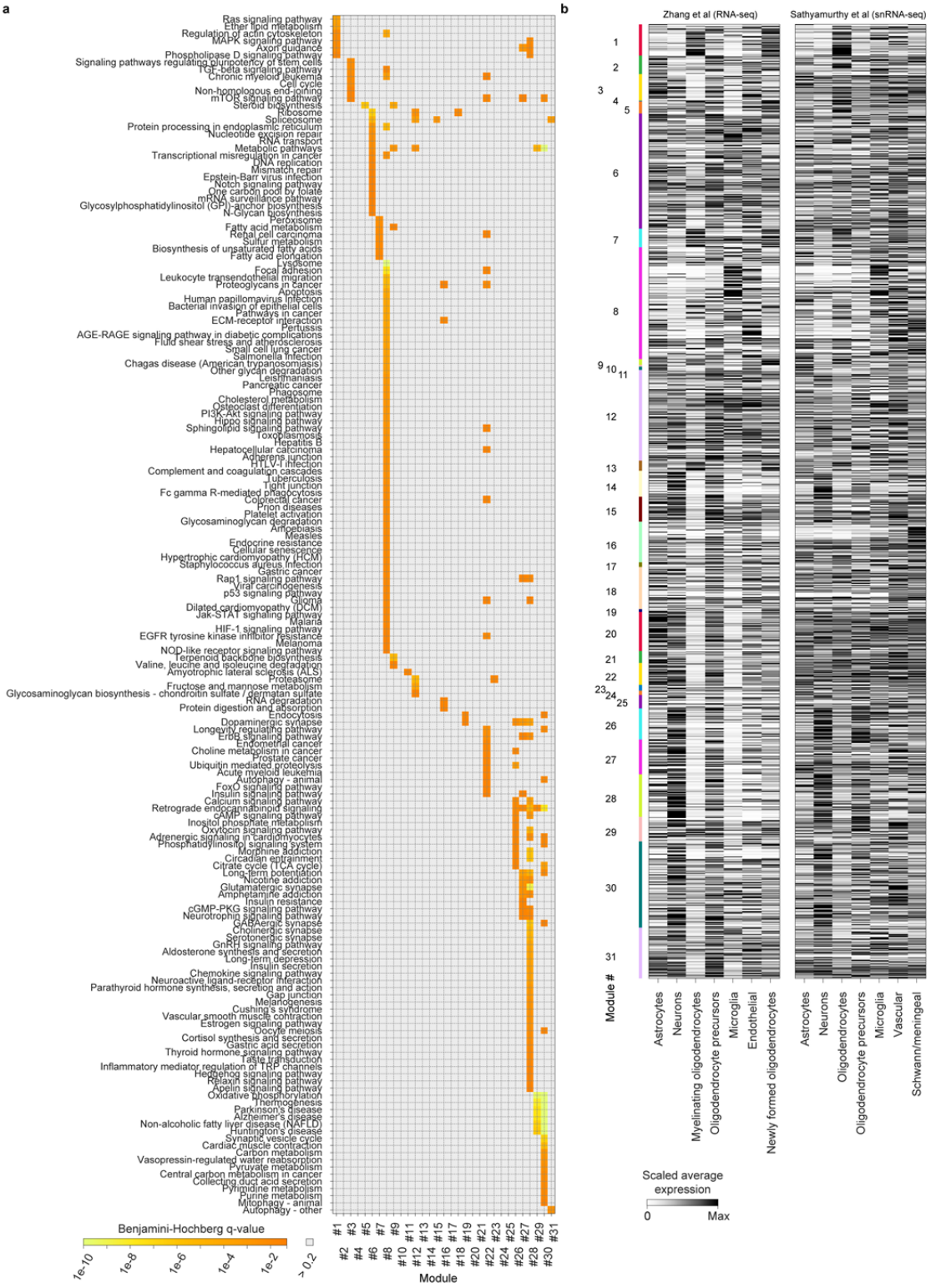

Extended Data Fig. 7 | Analysis of co-expression modules using KEGG pathways and cell type specific expression data. (**a**) Analysis of enriched KEGG pathways among the genes of the modules depicted in Fig. 3a (one-tailed Fisher's exact test with Benjamini-Hochberg correction, FDR < 0.1). The heatmap visualizes the adjusted p-values per KEGG category per module. Only the KEGG pathways enriched in at least one module are listed. The module identifiers listed on x axis match to the ones listed in Fig. 3a. (**b**) Overlay of cell type specific expression data on the co-expression modules of Fig. 3a. The heatmaps visualize scaled expression values. The scaled expression values are obtained per gene and per data set by dividing the expression values across cell types by the maximum expression value of that gene across the seven cell types. The order of the genes (rows) match to the order of rows of Fig. 3a.

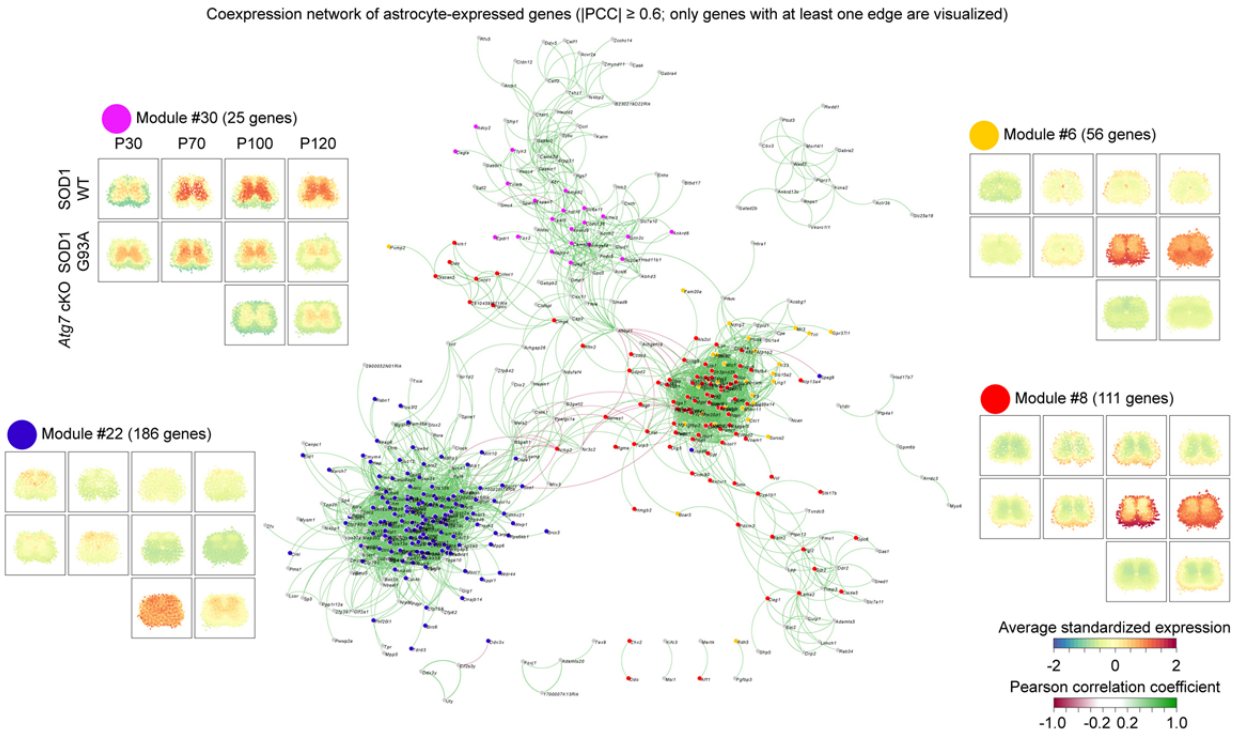

Extended Data Fig. 8 | Submodules that consist of astrocyte-expressed genes. Inferred co-expression network of astrocyte-expressed genes is illustrated. There is an edge between two genes if their absolute Pearson correlation coefficient is at least 0.6. Only the genes with at least one edge are visualized (Extended Data Table 7 has the full list of genes). The genes belonging to module 6, 8, 22, and 30 are highlighted in yellow, red, blue, and purple, respectively. Average spatiotemporal expression dynamics of the genes of the astrocyte submodules detected in co-expression modules 6 (yellow), 8 (red), 22 (blue), and 30 (purple) are visualized. The number of genes per co-expression module are listed.

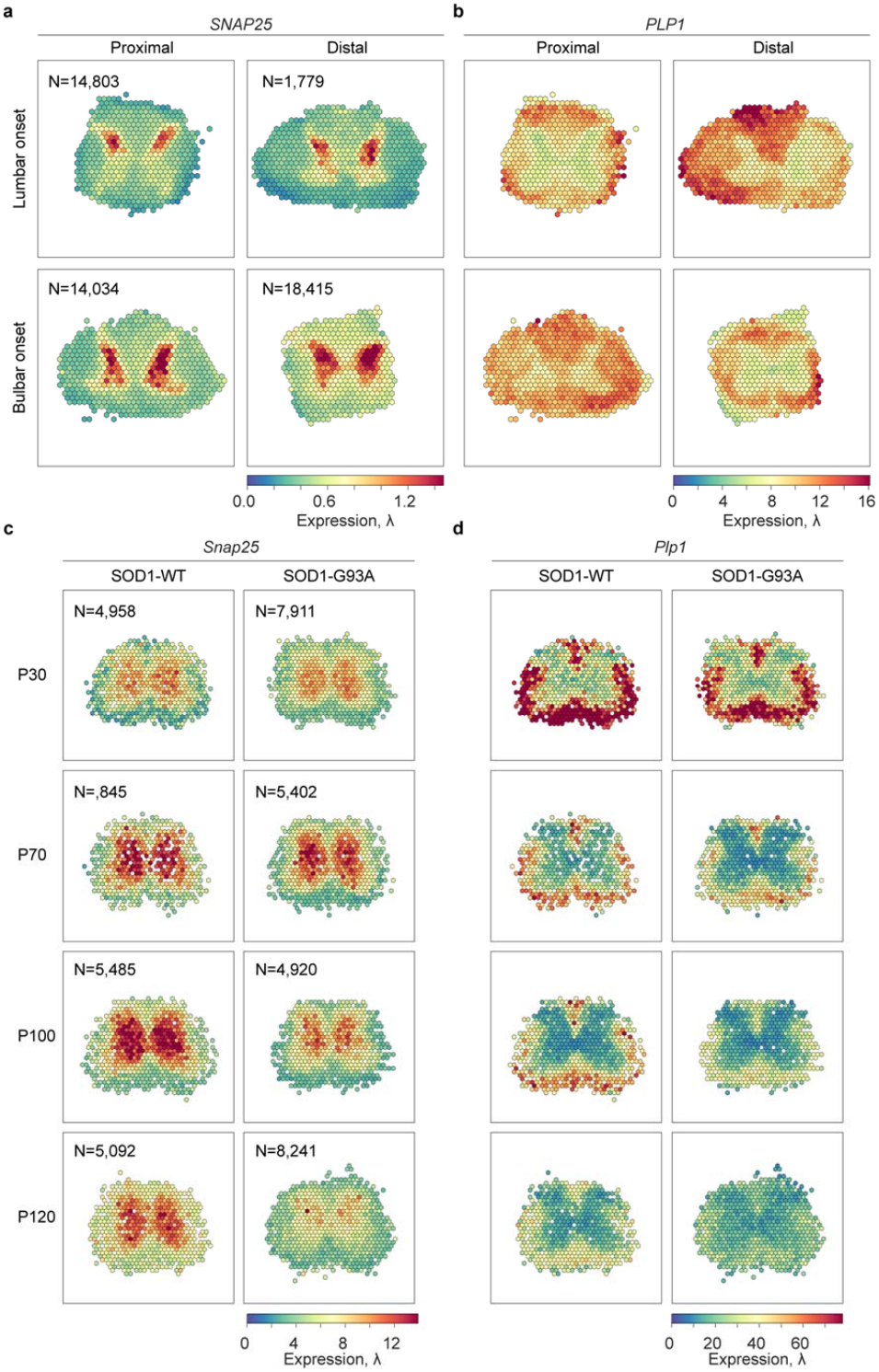

Extended Data Fig. 9 | Spatiotemporal expression dynamics of *Snap25* and *Plp1* in human and mouse spinal cords. (**a**) Spatial mRNA expression of *SNAP25* in lumbar onset (first row) and bulbar onset (second row) human spinal cords. The proximal (first column) and distal (second column) locations relative to onset are considered separately. The value of a bin is calculated as the mean of the ST values (posterior means of the rate parameters λ) within the bin area. Bins with less than 3 ST spots are discarded. The number of ST spots per condition are listed. (**b**) As in (**a**), with the focus here on *PLP1*. (**c**) Spatial mRNA expression of *Snap25* in SOD1-WT (left panel) and SOD1-G93A spinal cords (second panel) at P30 (first row), P70 (second row), P100 (third row), and P120 (fourth row). The value of a bin is calculated as the mean of the ST values (posterior means of the rate parameters λ) within the bin area. Bins with less than 3 ST spots are discarded. The number of ST spots per condition are listed. (**d**) As in (**c**), with the focus here on *Plp1*.

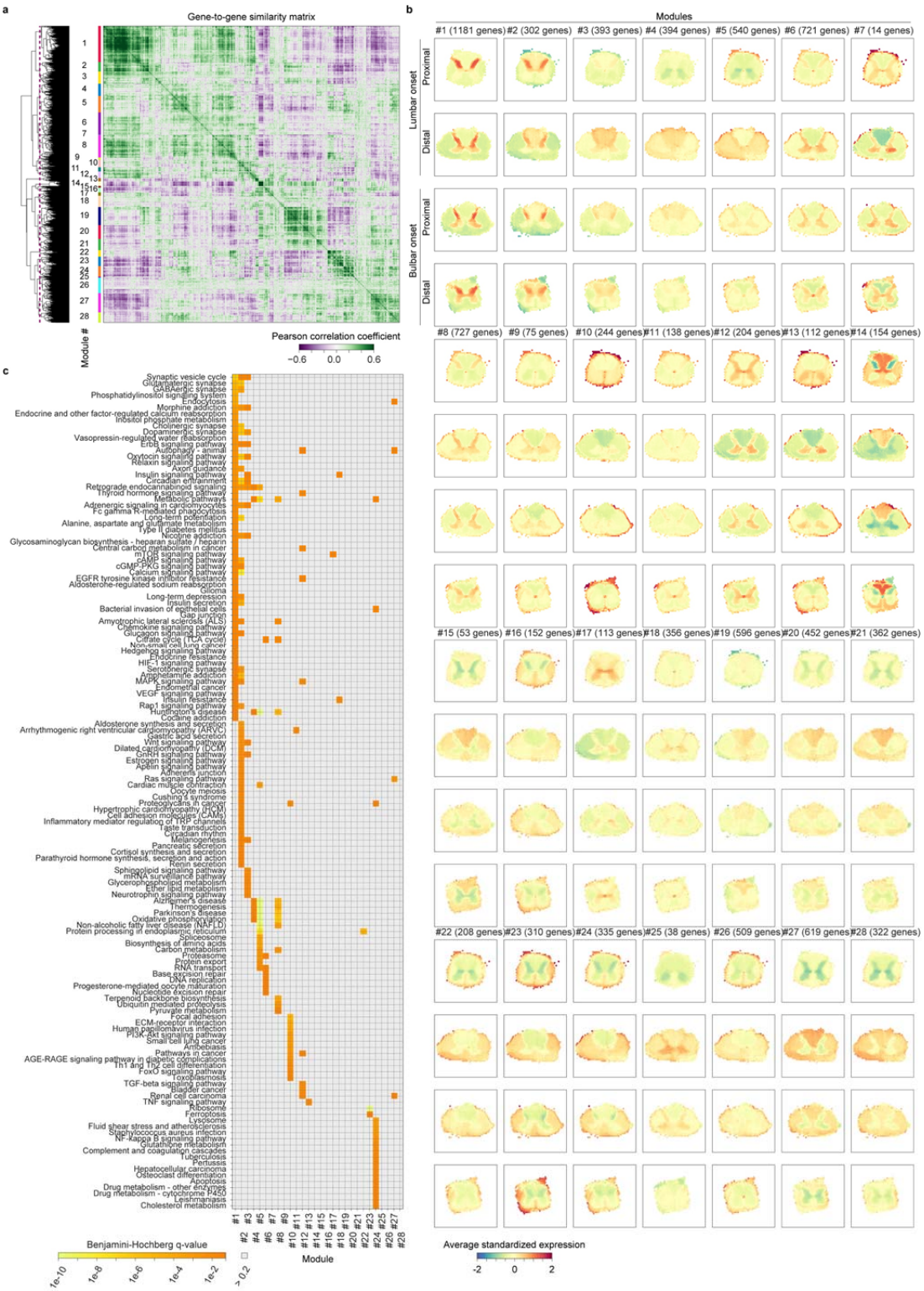

Extended Data Fig. 10 | Co-expression analysis of human ST data. (**a**) Biclustering of the human ST data of 9,624 genes and 61,031 ST spots set to reveal spatially and temporally co-expressed genes. The dashed vertical purple line in the dendrogram denotes the cutting point. The numerical identifiers given to the co-expression modules are listed on right of the dendrogram. (**b**) Average spatiotemporal expression dynamics of the genes of the co-expression modules of (**a**) are visualized. The number of genes per co-expression module are listed. (**c**) Analysis of enriched KEGG pathways among the genes of the modules depicted in (**a**) (one-tailed Fisher's exact test with Benjamini-Hochberg correction, FDR < 0.1). The heatmap visualizes the adjusted p-values per KEGG category per submodule. Only the KEGG pathways enriched in at least one submodule are listed. The module identifiers listed on x axis match to the ones listed in (**a**).

Supplementary Table 1. Sample and annotation statistics. Number of mice/patients, tissue sections, and spots per condition are listed. Number of spots per AAR for mouse and human ST data are listed.

Supplementary Table 2. Differential expression results of comparisons between regions. Table contains differential expression results of comparisons between regions per gene per time point. For instance, we compared expression per gene between ventral horn and dorsal horn, and ventral horn against all the other 11 AARs. Bayes factors and posterior means and standard deviations of compared β distributions are listed.

Supplementary Table 3. Differential expression results of comparisons between conditions. Table contains differential expression results of comparisons between conditions per gene per time point. Bayes factors and posterior means and standard deviations of compared β distributions are listed.

Supplementary Table 4. Genes comprising the mouse co-expression modules. Genes comprising the modules illustrated in Fig. 3a are listed.

Supplementary Table 5. KEGG pathway analysis of mouse co-expression modules. Results of the analysis of enriched KEGG pathways among the genes comprising the modules depicted in Fig. 3a are listed. Only statistically significant KEGG pathways for each module are listed (one-tailed Fisher's exact test with Benjamini-Hochberg correction, FDR < 0.1).

Supplementary Table 6. Mouse coexpression submodules and their KEGG pathway analysis results. Genes of the submodules together with their cell-type expression values are listed. Results of the analysis of enriched KEGG pathways among the genes comprising the

submodules are listed. Only statistically significant KEGG pathways for each module are listed (one-tailed Fisher's exact test with Benjamini-Hochberg correction, FDR < 0.1).

Supplementary Table 7. Astrocyte-enriched submodules. Genes comprising the submodules enriched in astrocyte-expressed genes are listed (Methods).

Supplementary Table 8. Genes comprising the human co-expression modules. Genes comprising the modules illustrated in Supplementary Fig. 10a are listed.

Supplementary Table 9. KEGG pathway analysis of human co-expression modules. Results of the analysis of enriched KEGG pathways among the genes comprising the modules depicted in Fig. 3a are listed. Only statistically significant KEGG pathways for each module are listed (one-tailed Fisher's exact test with Benjamini-Hochberg correction, FDR < 0.1).

Supplementary Table 10. Ventral horn coefficient differences. The posterior means of the human ventral horn coefficient difference (Δ_β) distributions (distal-proximal). The differences of the human coefficients are calculated within patients. Only genes that show consistent pattern across patients are listed. Posterior means of the ventral horn mouse coefficient difference (Δ_β) (between SOD1-WT and SOD1-G93A) distributions are listed.

Supplementary Methods. Our statistical model for analyzing spatial transcriptomics data. Provides a mathematical introduction to elements of our model, including hierarchical zero-inflated Poisson models, Poisson generalized linear models, and conditional autoregressive models. We then outline our hierarchical probabilistic model for spatial transcriptomics data and detail its application to human and mouse data.

Supplementary Methods: Spatiotemporal Dynamics of Molecular Pathology in Amyotrophic Lateral Sclerosis

Here we describe our statistical model for analyzing spatial transcriptomics (ST) data. First, we provide a mathematical introduction to introduce elements of our core model, including hierarchical zero-inflated Poisson (ZIP) models, Poisson generalized linear models, and conditional autoregressive (CAR) models. Following this introduction we will outline our hierarchical probabilistic model for spatial transcriptomics data and detail its application to both human and mouse ST data sets.

Background

Zero-inflated Poisson likelihood

Here we model transcriptome count data as a Poisson process interacting (hierarchically) with other model components. An appropriate Poisson model that can be used to model this core count process can be stated as (Gelman et al., 2013)

$$\begin{aligned} \lambda|\alpha_\lambda &\sim \Gamma(\alpha_{\lambda 1}, \alpha_{\lambda 2}), \\ y|\lambda &\sim \text{Poisson}(\lambda), \end{aligned} \tag{1}$$

where the rate parameter λ has a Gamma prior with parameters $\alpha_{\lambda 1}$ and $\alpha_{\lambda 2}$. Here the rate represents λ the underlying level (rate) of transcription (the latent value of interest in ST), and y represents the observed counts.

A key problem in ST and single cell genomics are small sample sizes (per location and cell respectively) and technical biases leading to high rates of missing data, termed here 'zero inflation'. Notably, the traditional Poisson model defined in Equation (1) fails in the cases where we have more zero-valued observations than expected from a Poisson model (Lambert, 1992). To account for an expected inflation of zeros, the following extension of the aforementioned

hierarchical Poisson model has been proposed (Lambert, 1992)

$$\begin{aligned} \theta^p|\alpha_p &\sim \text{Beta}(\alpha_{p1}, \alpha_{p2}), \\ \theta|\theta^p &\sim \text{Bernoulli}(\theta^p), \\ \lambda|\alpha_\lambda &\sim \Gamma(\alpha_{\lambda 1}, \alpha_{\lambda 2}), \\ y|\theta, \lambda &\sim \begin{cases} y = 0 & \text{if } \theta = 1 \\ y \sim \text{Poisson}(\lambda) & \text{if } \theta = 0 \end{cases}. \end{aligned} \tag{2}$$

That is, the hierarchical zero-inflated Poisson model (ZIP) given in Equation (2) consists two components: 1) a component that generates zeros and 2) a component that generates counts according to a Poisson distribution. Notably, both of the components are able to emit zeros. Effectively, by using ZIP we have the ability to introduce more probability mass to the outcome of zero and an excess of observations, y, can be tolerated without inappropriately excessively dragging aggregate posterior estimates to zero.

Often, the mixture model described in Equation (2) is stated as follows

$$\begin{aligned} \theta^p|\alpha_p &\sim \text{Beta}(\alpha_{p1}, \alpha_{p2}), \\ \lambda|\alpha_\lambda &\sim \Gamma(\alpha_{\lambda 1}, \alpha_{\lambda 2}), \\ y|\lambda, \theta_p &\sim \text{ZIP}(\lambda, \theta^p). \end{aligned} \tag{3}$$

After marginalizing out the binary parameter θ, we can state the ZIP likelihood function as

$$p(y|\lambda, \theta^p) \begin{cases} \theta^p + (1 - \theta^p)\exp(-\lambda) & \text{if } y = 0 \\ (1 - \theta^p)\frac{\lambda^y \exp(-\lambda)}{y!} & \text{if } y > 0 \end{cases}, \tag{4}$$

where θ^p represents the probability of extra zeros. Importantly, the likelihood in Equation (4) does not contain any discrete parameters, and thus we can utilize Hamiltonian Monte Carlo (HMC) for obtaining posterior samples (Neal et al., 2011).

Exposure

The Poisson distribution and the ZIP distribution above are defined in terms of rate, where rate is events per exposure. For instance, observed transcript or UMI counts (count) depend on the overall sequencing depths (exposure). Therefore, for considering different exposures s_i in the model, we transform rate λ to counts y_i as follows

$$\lambda = \frac{y_i}{s_i} \Leftrightarrow y_i = \lambda s_i \tag{5}$$

Then, we can model outcomes $y_i, i = 1, 2, \ldots, N$ of different exposures, s_i, $i = 1, 2, \ldots, N$, as (Gelman et al., 2013)

$$y_i \sim \text{Poisson}(\lambda s_i), \tag{6}$$

where λ is a common rate parameter.

Poisson regression and fitting core count model

Poisson regression models include Poisson generalized linear models (GLMs) which assume that the logarithm (other link functions can be chosen) of the rate parameter of the Poisson likelihood, λ, can be modeled by a linear model (Cameron and Trivedi, 2013; Gelman et al., 2013). As an example, let us consider the following Poisson GLM

$$\log(\lambda) = \mathbf{x}^{\mathrm{T}}\beta, \tag{7}$$

where $\mathbf{x}$ is the design vector and β is the coefficient vector. Let us assume that we have tuples $(\mathbf{x}_i, y_i)$, $i = 1, 2, \ldots, N$ representing observations. Then the task is to infer β using data under some inference scheme, such as maximum likelihood or Bayesian inferences (Gelman et al., 2013).

Conditional autoregressive (CAR) prior

Conditional autoregressive (CAR) models have been popular in modeling spatial autocorrelation in spatial data (Gelfand and Vounatsou, 2003; Jin et al., 2005; Wilson et al., 2017). In more detail, CAR prior assumes that the value at a given location is conditional on the values of neighboring locations. Notably, how the neighborhood is defined is a modeling question. For example, neighbors could be defined as proximal spots on the array, or as spots in corresponding anatomical regions, or as spots that are proximal in a reconstructed z-axis in a common coordinate). Furthermore, let the random vector $\psi = (\psi_1, \psi_2, \ldots, \psi_N)^{\mathrm{T}}$ represent N locations with a CAR prior. Then, the CAR prior of ψ can be expressed via conditional distributions

$$\psi_i | a, \mathbf{B}, \tau_i, \psi_{-i} \sim \mathcal{N}\left(a \sum_{j \in -i} b_{ij}\psi_j, \tau_i^{-1}\right), \; i = 1, 2, \ldots, N, \tag{8}$$

where τ_i are the conditional precision parameters, $a \in [0, 1)$ is a positive spatial autocorrelation parameter, $\mathbf{B} = \{b_{ij}\}$ where $b_{ii} = 0$, and $-i = \{j | j \in \{1, 2, \ldots, N\} \wedge j \neq i\}$ (Joseph, 2016). The joint distribution of ψ can obtained using Brook's lemma

$$\psi | a, \mathbf{B}, \mathbf{D}_\tau \sim \mathcal{N}\left(\mathbf{0}, \left(\mathbf{D}_\tau \left(\mathbf{I} - a\mathbf{B}\right)\right)^{-1}\right), \tag{9}$$

where $\mathbf{D}_\tau = \mathrm{diag}(\tau_1, \tau_2, \ldots, \tau_N)$ (Joseph, 2016). The following condition ensures that $\mathbf{D}_\tau(\mathbf{I} - a\mathbf{B})$ is a symmetric matrix (Gelfand and Vounatsou, 2003)

$$b_{ij}\tau_i = b_{ji}\tau_j, \; \forall i, j. \tag{10}$$

Next, let us introduce a computationally attractive CAR prior well suited to modeling the spatial coordinate (and other similarity relationships) present in integrated (multiple slices to make a z-axis) ST data sets (Joseph, 2016). Let

$\mathbf{W} = \{w_{ij}\}$ be the adjacency matrix representing neighborhood structure of the locations be defined by

$$w_{ij} = \begin{cases} 1 & \text{if } i \text{ is a neighbor of } j \text{ and } i \neq j \\ 0 & \text{otherwise} \end{cases}. \tag{11}$$

Clearly, the number of neighbors of location i is then $m_i = \sum_{j=1}^{N} w_{ji}$. Moreover, let us assume $\mathbf{D} = \text{diag}(m_1, m_2, \ldots, m_N)$. Additionally, let us assume $\mathbf{D}_\tau = \tau\mathbf{D}$ and $\mathbf{B} = \mathbf{D}^{-1}\mathbf{W}$. Then, the joint distribution of ψ simplifies to (Joseph, 2016)

$$\psi | a, \tau, \mathbf{W} \sim \mathcal{N}\left(\mathbf{0}, \left(\tau\left(\mathbf{D} - a\mathbf{W}\right)\right)^{-1}\right). \tag{12}$$

Note that every location has to have at least one neighbor and the matrix $\mathbf{D}$ can be calculated from the adjacency matrix $\mathbf{W}$. Importantly, this CAR prior can be implemented effectively in Stan (Carpenter et al., 2017) by exploiting sparse matrix multiplication and a fast determinant solving approach (Jin et al., 2005; Joseph, 2016).

Statistical analysis of ST data

Notations

Let there be N_{genes} genes and N_{tissues} tissue sections. Moreover, let us denote the number of spots on j^{th} tissue section as $N_{\text{spots}}^{(j)}$. Then, the total number of spots over tissues is $N_{\text{spots}} = \sum_{j=1}^{N_{\text{tissues}}} N_{\text{spots}}^{(j)}$.

The number of reads for i^{th} gene on j^{th} tissue at k^{th} spot is denoted as $y_{i,j,k}$. Then, the total number of gene reads, $M_{j,k}$, on j^{th} tissue at k^{th} spot is $M_{j,k} = \sum_{i}^{N_{\text{genes}}} y_{i,j,k}$. The annotation information of kth spot on j^{th} tissue is one hot encoded in $\mathbf{x}_{j,k} \in \{0,1\}^{11}$.

Finally, for notational purposes, let $\rho(m, s, g, t)$ be a bijective function $\mathbb{N}^4 \to \mathbb{N}$ that maps mouse, sex, genotype, and time point indices to a unique tissue section index. Whereas in human, we define a bijective function $\rho : \mathbb{N}^3 \to \mathbb{N}$ that maps onset (o), location (l), and human (h) indices to a unique tissue section index. These functions are used in the model definition to simplify the indexing of the coefficient vectors; that is, we can reference coefficient vectors with a unique tissue specific index j as $\beta_{i,\rho^{-1}(j)}$, or with mouse (m), sex (s), genotype (g), and time point (t) indices as $\beta_{i,m,s,g,t}$.

Overview

To model spatial gene expression distributions using ST data, we formulate a hierarchical generative zero-inflated Poisson regression model. To improve parameter estimates, we wish to analyze multiple tissue sections together. A straight-forward analysis of replicates at the level of individual spot is impractical: 1) the spot locations vary between tissue sections, 2) compositions of cell

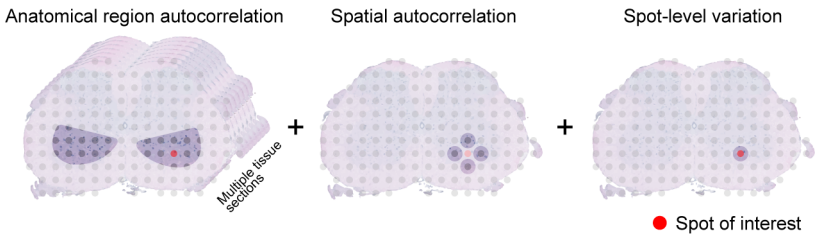

Figure 1: Our schema to decompose variation per gene in ST data into three components. Using spot annotations we can share information across multiple tissue sections to estimate latent expression values of anatomical regions (left). Additionally, we aim to estimate local spatial autocorrelation (middle). Remaining variation is accounted at the level of individual spots. Note that in practice all spots are analyzed simultaneously.

types are likely vary between tissue sections, 3) random sampling of a small subset of mRNA molecules, and 4) UMI counts are low. Therefore, our regression model has a linear component that allows us to integrate data across multiple tissue sections via annotations of the spots based on their location on the tissue (anatomical regions). In addition, we include a CAR component that allows us to consider spatial correlation and a spot-level component to capture variation at the level of individual spots (Figure 1).

Model components

We construct our linear model based on the annotations of the spots obtained through their location on the tissue. Clearly, the number of annotation categories depends on the tissue type and the biological question, and it balances between spatial resolution and number of samples. In this study, we use 11 different anatomical regions decided on the basis of known major functional divisions of spinal cord (Extended Data Figure 2a). Notably, our linear model construct has many advantages: first, the annotations-based linear model enables us to model quick changes in tissue type, which might be tricky to handle with Gaussian random fields and similar approaches, and second, it enables us to simultaneously consider spots across multiple tissue sections at the annotation category level, leading to more reliable estimations at the annotation category level. The contribution of the linear model component can be simply stated as $\mathbf{x}_{j,k}^{\mathrm{T}}\beta$ where the vector $\mathbf{x}_{j,k} \in \{0,1\}^{11}$ has one hot encoded annotation of kth spot on j^{th} tissue section and the vector $\beta \in \mathbb{R}^{11}$ contains coefficients representing latent expression levels of anatomical regions. Importantly, we encode our experimental design in the linear model through multilevel modeling of β, and thus estimate latent expression levels and quantify variation at different levels (e.g. between sexes and individuals). Notably, we use different multilevel linear models for analyzing human and mouse ST data to reflect the differences in the

experimental designs.

The assumption of gene expression uniformity within an annotation category is biologically unrealistic when estimating gene expression at the level of individual spot. To overcome this restriction, we incorporate a CAR component, for sharing information between nearby spots, at the level of individual tissue section in the model, $\psi_{i,j}$. These CAR components capture spatial autocorrelation not explained by the linear component. To use the CAR model, we first have to define the neighbor structure of the spots; in this study, we assume that the neighbors of a given spot are its adjacent present spots on the two-dimensional lattice (4-neighborhood).

Due to intrinsic biological variation there is expected to be independent variation at the level of individual spots. To take this type of variation into account, we consider spot-level variations $\epsilon_{i,j,k}$ not captured neither by the linear nor the CAR components.

To take into account spots' different exposures, we use sequencing depth as a proxy to the exposure and calculate the exposures $s_{j,k}$ as

$$s_{j,k} = \frac{M_{j,k}}{\text{median}(\{M_{j,k_j} | j = 1, 2, \ldots, N_{\text{tissues}}, k_j = 1, 2, \ldots, N^{(j)}_{\text{spots}})}. \tag{13}$$

As a consequence of estimating exposure from sequencing depth, we will not be modeling absolute gene expression (numbers of messenger RNA molecules) levels across spots. Moreover, all the exposures $s_{j,k}$ are positive. Additionally, the exposure of the sample with the median sequencing depth is 1, whereas the exposures of the samples with greater sequencing depth than the median are greater than 1.

Prior definitions

The coefficient vector $\beta_{i,g,t}$ is given a weakly informative Gaussian prior ($\beta_{i,g,t} \sim \mathcal{N}(\mathbf{0}, 2^2\mathbf{I})$). The parameters σ_i^{sex} and σ_i^{mouse} representing variation between sexes and mice, respectively, are given truncated Gaussian priors ($\sigma_i^{\text{sex}}, \sigma_i^{\text{mouse}} \sim \mathcal{N}_{\geq 0}(0, 1)$) reflecting our ignorance of the level of variation. The parameter θ_i^p representing the probability of extra zeros is given a weakly informative Beta prior ($\theta^p \sim \text{Beta}(1, 2)$) which is slightly skewed towards zero. The spatial autocorrelation parameter a_i is given a uniform prior between 0 and 1 ($a_i \sim \mathcal{U}(0, 1)$). The conditional precision parameter τ_i is assigned a weakly informative inverse Gamma prior ($\tau_i \sim \Gamma^{-1}(1, 1)$). Finally, the parameter $\epsilon_{i,j,k}$ representing spot-level variation is given a hierarchical Gaussian prior ($\epsilon_{i,j,k} | \sigma_i \sim \mathcal{N}_{\geq 0}(0, \sigma_i^2)$), where σ_i is given a truncated Gaussian prior ($\sigma_i \sim \mathcal{N}_{\geq 0}(0, 0.3^2)$ supporting relatively low levels of variation.

Definition

The resulting statistical model (Figure 2) used to analyze mouse ST data outlined above can be formally defined as follows

$$
\begin{aligned}
\sigma_i^{\text{sex}}|\alpha_\sigma &\sim \mathcal{N}_{\geq 0}(0,1),\\
\sigma_i^{\text{mouse}}|\alpha_\sigma &\sim \mathcal{N}_{\geq 0}(0,1),\\
\beta_{i,g,t}|\alpha_\beta &\sim \mathcal{N}(\mathbf{0}, 2^2\mathbf{I}),\\
\beta_{i,s,g,t}|\beta_{i,g,t}, \sigma_i^{\text{sex}} &\sim \mathcal{N}(\beta_{i,g,t}, \sigma_i^{\text{sex}2}\mathbf{I}),\\
\beta_{i,m,s,g,t}|\beta_{i,s,g,t}, \sigma_i^{\text{mouse}} &\sim \mathcal{N}(\beta_{i,s,g,t}, \sigma_i^{\text{mouse}2}\mathbf{I}),\\
a_i|\alpha_a &\sim \mathcal{U}(0,1),\\
\tau_i|\alpha_\tau &\sim \Gamma^{-1}(1,1),\\
\psi_{i,j}|a_i, \tau_i, \mathbf{W}_j &\sim \mathcal{N}\left(\mathbf{0}, (\tau_i(\mathbf{D}_j - a_i\mathbf{W}_j))^{-1}\right),\\
\sigma_i|\alpha_\epsilon &\sim \mathcal{N}_{\geq 0}(0, 0.3^2),\\
\epsilon_{i,j,k}|\sigma_i &\sim \mathcal{N}(0, \sigma_i^2),\\
\lambda_{i,j,k} &= \exp\left(\mathbf{x}_{j,k}^{\mathrm{T}}\beta_{i,\rho^{-1}(j)} + \psi_{i,j,k} + \epsilon_{i,j,k}\right),\\
\theta_i^p|\alpha_p &\sim \text{Beta}(1,2),\\
y_{i,j,k} &\sim \text{ZIP}(s_{j,k}\lambda_{i,j,k}, \theta_i^p),
\end{aligned}
\tag{14}
$$

where $i = 1, 2, \ldots, N_{\text{genes}}$, $j = 1, 2, \ldots, N_{\text{tissues}}$, and $k = 1, 2, \ldots, N_{\text{spots}}^{(j)}$.

The graphical representation of the model described in Equation (14) is illustrated in Figure 2. The posterior distribution function of Equation (14) is proportional to the product of prior probability density functions and likelihood function

$$
\begin{aligned}
&p(\beta, \psi_{i,:}, a_i, \tau_i, \sigma_i, \sigma_i^{\text{sex}}, \sigma_i^{\text{mouse}}, \epsilon_{i,:,:}, \theta_i^p, |\alpha, \mathbf{W}, \mathbf{X}, \mathbf{s}) \propto\\
&p(\sigma_i^{\text{sex}}|\alpha_\sigma)p(\sigma_i^{\text{mouse}}|\alpha_\sigma)p(\sigma_i|\alpha_\epsilon)p(\tau_i|\alpha_\tau)p(\theta_i^p|\alpha_p)p(a_i|\alpha_a)\\
&\left[\prod_{g=1}^{N_{\text{genotypes}}}\prod_{t=1}^{N_{\text{timepoints}}}\left[p(\beta_{i,g,t}|\alpha_\beta)\right.\right.\\
&\left.\left.\left[\prod_{s=1}^{N_{\text{sexes}}^{(g,t)}}\left[p(\beta_{i,s,g,t}|\beta_{i,g,t}, \sigma_i^{\text{sex}})\prod_{m=1}^{N_{\text{mice}}^{(s,g,t)}} p(\beta_{i,m,s,g,t})|\beta_{i,s,g,t}, \sigma_i^{\text{mouse}})\right]\right]\right]\right]\\
&\left[\prod_{j=1}^{N_{\text{tissues}}}\prod_{k=1}^{N_{\text{spots}}^{(j)}} p(\epsilon_{i,j,k}|\sigma_i)\right]\\
&\left[\prod_{j=1}^{N_{\text{tissues}}} p(\psi_{i,j}|\alpha_i, \tau_i, \mathbf{W}_j)\right]\left[\prod_{j=1}^{N_{\text{tissues}}}\prod_{k=1}^{N_{\text{spots}}^{(j)}} p(y_{i,j,k}|\lambda_{i,j,k}, s_{j,k}, \theta_i^p)\right],
\end{aligned}
\tag{15}
$$

where $\beta = (\beta_{i,:,:}, \beta_{i,:,:,:}, \beta_{i,:,:,:,:})$, $\alpha = (\alpha_\beta, \alpha_\sigma, \alpha_a, \alpha_\tau, \alpha_\epsilon, \alpha_p)$, $\mathbf{W} = \{W_j | j =$

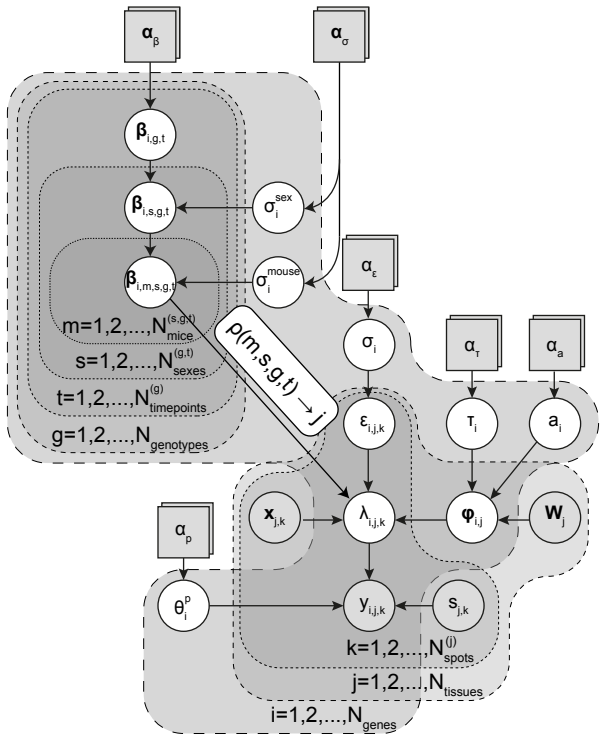

$$\lambda_{i,j,k} = \exp\left(\mathbf{x}_{j,k}^{\mathrm{T}}\beta_{i,\rho^{-1}(j)} + \psi_{i,j,k} + \epsilon_{i,j,k}\right)$$

Figure 2: A graphical representation of the statistical model used to analyze mouse ST data. The white and grey circles represent observed and latent variables, respectively. The grey squares represent user-definable parameters that define prior distributions of latent variables. The plates represent repetitions of different parts of the model, for example, in each gene has its own θ_i^p and each tissue section has its own spot adjacency matrix $\mathbf{W}_j$. The left part of the model constructed around β random variables represents the linear model component. Whereas, the model branches governing the random variables ψ and ϵ are the spatial random effect and spot-level variation components, respectively. The parameters σ_i^{sex} and $\sigma_i^{\mathrm{mouse}}$ capture variation between sexes and mice, respectively. For instance, $\beta_{i,g,t}$ and σ_i^{sex} define the distribution of $\beta_{i,s,g,t}$. For visualization purposes, the function ρ is used to map g (genotype), t (time point), s (sex), and m (mouse) indices to a single tissue section index j.

$1, 2, \ldots, N_{\text{tissues}}\}$, $\mathbf{X} = \{x_{j,k} | j = 1, 2, \ldots, N_{\text{tissues}} \wedge k = 1, 2, \ldots, N_{\text{spots}}^{(j)}\}$, and $\mathbf{s} = \{s_{j,k} | j = 1, 2, \ldots, N_{\text{tissues}} \wedge k = 1, 2, \ldots, N_{\text{spots}}^{(j)}\}$.

The statistical model used to analyze human ST data has only minor changes in the linear model component, with the principle change being that we do not condition on sex, that we directly model donor effect, and that we do not model time and genotype (as the limitations of the clinical setting make including these dimensions in the design impractical).

$$
\begin{aligned}
\sigma_i^{\text{human}} | \alpha_\sigma &\sim \mathcal{N}_{\geq 0}(0, 1), \\
\beta_{i,o,l} | \alpha_\beta &\sim \mathcal{N}(\mathbf{0}, 2^2 \mathbf{I}), \\
\beta_{i,h,o,l} | \beta_{i,o,l}, \sigma_i^{\text{human}} &\sim \mathcal{N}(\beta_{i,o,l}, {\sigma_i^{\text{human}}}^2 \mathbf{I}), \\
a_i | \alpha_a &\sim \mathcal{U}(0, 1), \\
\tau_i | \alpha_\tau &\sim \Gamma^{-1}(1, 1), \\
\psi_{i,j} | a_i, \tau_i, \mathbf{W}_j &\sim \mathcal{N}\left(\mathbf{0}, \left(\tau_i \left(\mathbf{D}_j - a_i \mathbf{W}_j\right)\right)^{-1}\right), \\
\sigma_i | \alpha_\epsilon &\sim \mathcal{N}_{\geq 0}(0, 0.3^2), \\
\epsilon_{i,j,k} | \sigma_i &\sim \mathcal{N}(0, \sigma_i^2), \\
\lambda_{i,j,k} &= \exp\left(\mathbf{x}_{j,k}^{\text{T}} \beta_{i,\rho^{-1}(j)} + \psi_{i,j,k} + \epsilon_{i,j,k}\right), \\
\theta_i^p | \alpha_p &\sim \text{Beta}(1, 2), \\
y_{i,j,k} &\sim \text{ZIP}(s_{j,k} \lambda_{i,j,k}, \theta_i^p),
\end{aligned}
\tag{16}
$$

where $i = 1, 2, \ldots, N_{\text{genes}}$, $j = 1, 2, \ldots, N_{\text{tissues}}$, and $k = 1, 2, \ldots, N_{\text{spots}}^{(j)}$. The graphical model of Equation (16) is illustrated in Figure 3. Furthermore, the posterior distribution function of Equation (16) is

$$
\begin{aligned}
p(\beta_{i,:,:}, \beta_{i,:,:,:}, \psi_{i,:}, a_i, \tau_i, \sigma_i, \sigma_i^{\text{human}}, \epsilon_{i,:,:}, \theta_i^p, | \alpha, \mathbf{W}, \mathbf{X}, \mathbf{s}) &\propto \\
p(\sigma_i^{\text{human}} | \alpha_\sigma) p(\sigma_i | \alpha_\epsilon) p(\tau_i | \alpha_\tau) p(\theta_i^p | \alpha_p) p(a_i | \alpha_a) & \\
\left[\prod_{o=1}^{N_{\text{onsets}}} \prod_{l=1}^{N_{\text{locations}}} \left[p(\beta_{i,o,l} | \alpha_\beta) \left[\prod_{h=1}^{N_{\text{humans}}^{(o,l)}} p(\beta_{i,h,o,l}) | \beta_{i,o,l}, \sigma_i^{\text{human}})\right]\right]\right] & \\
\left[\prod_{j=1}^{N_{\text{tissues}}} \prod_{k=1}^{N_{\text{spots}}^{(j)}} p(\epsilon_{i,j,k} | \sigma_i)\right] \left[\prod_{j=1}^{N_{\text{tissues}}} p(\psi_{i,j} | \alpha_i, \tau_i, \mathbf{W}_j)\right] & \\
\left[\prod_{j=1}^{N_{\text{tissues}}} \prod_{k=1}^{N_{\text{spots}}^{(j)}} p(y_{i,j,k} | \lambda_{i,j,k}, s_{j,k}, \theta_i^p)\right], &
\end{aligned}
\tag{17}
$$

where $\alpha = (\alpha_\beta, \alpha_\sigma, \alpha_a, \alpha_\tau, \alpha_\epsilon, \alpha_p)$, $\mathbf{W} = \{W_j | j = 1, 2, \ldots, N_{\text{tissues}}\}$, $\mathbf{X} = \{x_{j,k} | j = 1, 2, \ldots, N_{\text{tissues}} \wedge k = 1, 2, \ldots, N_{\text{spots}}^{(j)}\}$, and $\mathbf{s} = \{s_{j,k} | j = 1, 2, \ldots, N_{\text{tissues}} \wedge k = 1, 2, \ldots, N_{\text{spots}}^{(j)}\}$.

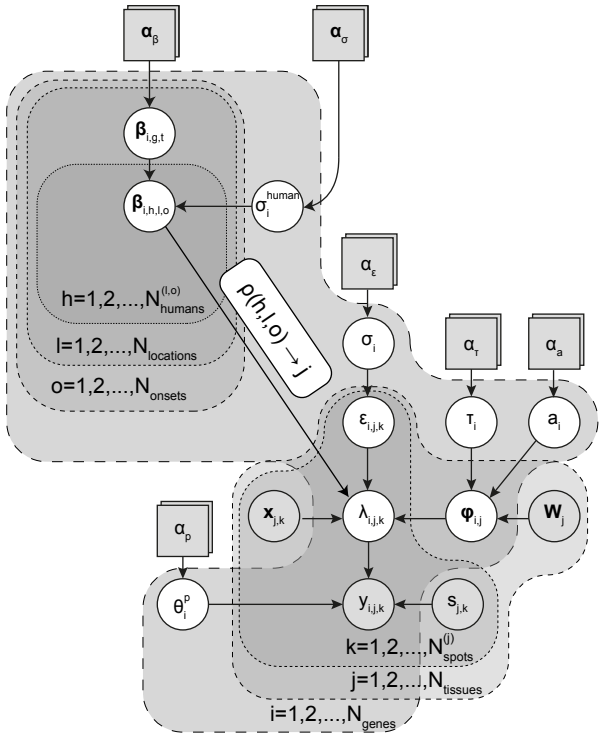

$$\lambda_{i,j,k} = \exp\left(\mathbf{x}_{j,k}^{\mathrm{T}}\beta_{i,\rho^{-1}(j)} + \psi_{i,j,k} + \epsilon_{i,j,k}\right)$$

Figure 3: A graphical representation of the statistical model used to analyze human ST data. The white and grey circles represent observed and latent variables, respectively. The grey squares represent user-definable parameters that define prior distributions of latent variables. The plates represent repetitions of different parts of the model, for example, in each gene has its own θ_i^p and each tissue section has its own spot adjacency matrix $\mathbf{W}_j$. The left part of the model constructed around β random variables represents the linear model component. Whereas, the model branches governing the random variables ψ and ϵ are the spatial random effect and spot-level variation components, respectively. The parameter σ_i^{human} captures variation between humans. For instance, $\beta_{i,l,o}$ and σ_i^{human} define the distribution of $\beta_{i,h,l,o}$. For visualization purposes, the function ρ is used to map o (onset), l location, and h (human) indices to a single tissue section index j.

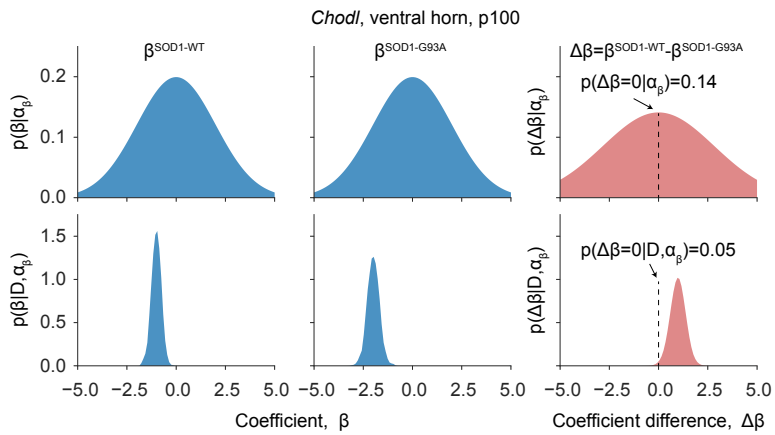

Figure 4: The prior distributions of $\beta^{(1)}$ (on left), $\beta^{(1)}$ (on middle), and $\Delta\beta = \beta^{(1)} - \beta^{(2)}$ (on right) are illustrated in the top row, whereas, the posterior distributions of the corresponding random variables are visualized in the bottom row in the same order. The prior and posterior densities at $\Delta\beta = 0$ are listed on right; in this example the Bayes factor is be approximately 2.8.

Detecting differential expression from ST data

In many biological applications, we wish to quantify differential gene expression between various conditions; for instance, between different genotypes, time points, or spatial annotation categories. As mentioned above, we can do this by studying the estimated β coefficients. First, let us assume without loss of generality that we want to quantify the difference between $\beta^{(1)}$ and $\beta^{(2)}$ representing two different conditions. Next, let us define a random variable $\Delta_\beta = \beta^{(1)} - \beta^{(2)}$, which captures the difference of $\beta^{(1)}$ and $\beta^{(2)}$. For instance, if the distribution of Δ_β is tightly centered around zero, then the distributions of $\beta^{(1)}$ and $\beta^{(2)}$ are highly similar to each other. To interpret the $\Delta_\beta|\mathcal{D}, \alpha_\beta$ (a posteriori), we compare it with $\Delta_\beta|\alpha_\beta$ (a priori). Formally, this comparison is done using the Savage-Dickey density ratio that approximates Bayes factors (Dickey, 1971; Wagenmakers et al., 2010)

$$\mathrm{BF} \approx \frac{p(\Delta_\beta = 0|\alpha_\beta)}{p(\Delta_\beta = 0|\mathcal{D}, \alpha_\beta)}, \tag{18}$$

where the probability density functions are evaluated at zero. The aforementioned Savage-Dickey procedure is graphically illustrated in Figure 4. The Savage-Dickey density ratio has been used previously for detecting alternative splicing and differential methylation from posterior distributions (Katz et al., 2010; Äijö et al., 2016) Importantly, $p(\Delta_\beta|\alpha_\beta)$ can be derived analytically, whereas, $p(\Delta_\beta|\mathcal{D}, \alpha_\beta)$ has to approximated using the obtained posterior samples.

References

Tarmo Äijö, Yun Huang, Henrik Mannerström, Lukas Chavez, Ageliki Tsagaratou, Anjana Rao, and Harri Lähdesmäki. A probabilistic generative model for quantification of dna modifications enables analysis of demethylation pathways. *Genome Biology*, 17(1):1–22, 2016. ISSN 1474-760X. doi: 10.1186/s13059-016-0911-6. URL `http://dx.doi.org/10.1186/s13059-016-0911-6`.

A Colin Cameron and Pravin K Trivedi. *Regression analysis of count data*, volume 53. Cambridge university press, 2013.

Bob Carpenter, Andrew Gelman, Matthew Hoffman, Daniel Lee, Ben Goodrich, Michael Betancourt, Marcus Brubaker, Jiqiang Guo, Peter Li, and Allen Riddell. Stan: A probabilistic programming language. *Journal of Statistical Software, Articles*, 76(1):1–32, 2017. ISSN 1548-7660. doi: 10.18637/jss.v076.i01. URL `https://www.jstatsoft.org/v076/i01`.

James M Dickey. The weighted likelihood ratio, linear hypotheses on normal location parameters. *The Annals of Mathematical Statistics*, pages 204–223, 1971.

Alan E Gelfand and Penelope Vounatsou. Proper multivariate conditional autoregressive models for spatial data analysis. *Biostatistics*, 4(1):11–15, 2003.

Andrew Gelman, John B Carlin, Hal S Stern, David B Dunson, Aki Vehtari, and Donald B Rubin. *Bayesian data analysis*. CRC press, 2013.

Xiaoping Jin, Bradley P Carlin, and Sudipto Banerjee. Generalized hierarchical multivariate car models for areal data. *Biometrics*, 61(4):950–961, 2005.

Max Joseph. Exact sparse CAR models in Stan, 2016. URL `http://mc-stan.org/users/documentation/case-studies/mbjoseph-CARStan.html`.

Yarden Katz, Eric T Wang, Edoardo M Airoldi, and Christopher B Burge. Analysis and design of rna sequencing experiments for identifying isoform regulation. *Nature methods*, 7(12):1009, 2010.

Diane Lambert. Zero-inflated poisson regression, with an application to defects in manufacturing. *Technometrics*, 34(1):1–14, 1992.

Radford M Neal et al. Mcmc using hamiltonian dynamics. *Handbook of Markov Chain Monte Carlo*, 2(11), 2011.

Eric-Jan Wagenmakers, Tom Lodewyckx, Himanshu Kuriyal, and Raoul Grasman. Bayesian hypothesis testing for psychologists: A tutorial on the savage–dickey method. *Cognitive psychology*, 60(3):158–189, 2010.

Andrew M Wilson, Daniel W Brauning, Caitlin Carey, and Robert S Mulvihill. Spatial models to account for variation in observer effort in bird atlases. *Ecology and Evolution*, 7(16):6582–6594, 2017.